



# Simulation of Taylor flow evaporation for bubble-pump applications



Alexander S. Rattner<sup>a</sup>, Srinivas Garimella<sup>b,\*</sup>

<sup>a</sup> Department of Mechanical and Nuclear Engineering, The Pennsylvania State University, University Park, PA 16802, United States

<sup>b</sup> George W. Woodruff School of Mechanical Engineering, Georgia Institute of Technology, Atlanta, GA 30318, United States

## ARTICLE INFO

### Article history:

Received 6 June 2017

Received in revised form 13 August 2017

Accepted 28 August 2017

Available online 15 September 2017

### Keywords:

Bubble pump

Volume of fluid

Flow boiling

Absorption refrigeration

## ABSTRACT

Single-pressure absorption systems incorporate bubble-pump generators (BPGs) for refrigerant separation and passive fluid circulation. In conventional spot-heated BPGs, heat is transferred over a small area, requiring high source temperatures. Distributed-heated BPGs receive thermal input over most of the component surface, enabling low temperature operation. In this investigation, a Volume-of-Fluid phase-change simulation formulation is developed and validated. This approach is applied to the evaporating Taylor flow pattern in distributed-heated BPGs. A 2-D axisymmetric simulation is performed, which yields detailed information about the developing heat transfer and two-phase flow phenomena. Results are used to assess predicted trends and sub-models from a 1-D segmented BPG model. Close agreement is obtained between segmented model and simulation results for bubble rise velocity (5–7% deviation), bubble and slug lengths, void fraction (3%), and hydrodynamic pressure drop (18%). Specifying average Taylor bubble lengths from the simulation as an input to the segmented model reduces hydrodynamic pressure drop deviation to 6%. Simulated flow-evaporation heat transfer coefficients are significantly higher than those predicted using analytic models from the literature. A new flow evaporation heat transfer correlation that accounts for developing slug flow effects is proposed, and yields close agreement with simulation results for heat transfer coefficient (AAD = 11%) and overall heat transfer rate (2%). Overall, this investigation provides validation for a distributed-heated BPG modeling approach, which can enable passive refrigeration for diverse applications.

© 2017 Elsevier Ltd. All rights reserved.

## 1. Introduction

### 1.1. Background

Bubble-pump generators (BPGs) are key components of single-pressure absorption refrigeration technologies, such as the diffusion absorption refrigeration (DAR) cycle. BPGs are usually configured as externally heated vertical tubes that receive liquid refrigerant-absorbent solution from a lower reservoir. External heat is supplied to desorb vapor refrigerant from the solution, and the buoyancy of rising bubbles pumps liquid through the BPG tube (Fig. 1). Thus, the BPG component separates the refrigerant stream and provides the hydrostatic head to drive solution flow through other components, enabling fully passive system operation. The liquid-vapor mixture usually flows through the BPG in the Taylor or slug flow regime [1].

Conventional BPGs are *spot heated* [2,3], with all heat transfer occurring over a small area near the base of the component (indicated in Fig. 1). This mode of operation enables high solution

pumping rates and simple analysis, as flow rates are uniform along the major portion of the component. However, these designs require high input temperatures (150–200 °C [4,5]), usually delivered with electrical resistance heaters or chemical fuel (e.g., propane). If the heat transfer area can be increased, then lower temperature thermal sources such as solar heat or engine waste heat can be employed. Recently, a number of investigations of *distributed-heated* BPGs in which heat transfer occurs over most of the component surface [4,6] have been performed. Rattner and Garimella [1] demonstrated stable distributed-heated operation of a steam-water BPG with thermal input only ~10 K above the fluid saturation temperature.

Few experimental or modeling studies have been conducted for distributed-heated BPGs. Experimental validation of models has primarily been global in nature, focusing on outlet flow rates and overall heat transfer. This approach does not provide local details of axially varying quantities (e.g., void fraction, pressure gradient, wall heat flux), and does not permit independent evaluation of sub-models. It is difficult to perform more detailed experimental investigations because the two-phase flow pattern develops continuously, and the need for external heat input and insulation may preclude optical access. However, by directly simulating these

\* Corresponding author.

E-mail address: [sgarimella@gatech.edu](mailto:sgarimella@gatech.edu) (S. Garimella).

## Nomenclature

$A$	area ( $\text{m}^2$ )	<i>Greek characters</i>	
$A_D$	diagonal entry in discretized momentum matrix equation ( $\text{kg m}^{-3} \text{s}^{-1}$ )	$\alpha$	void fraction
$Bo$	Bond number ( $(\rho_L - \rho_V)gD^2/\sigma$ )	$\alpha_1$	liquid-phase-fraction in a mesh cell
$C_0$	distribution parameter in bubble velocity model	$\alpha_{1,pc}$	phase-fraction volumetric source due to phase change ( $\text{s}^{-1}$ )
$Ca$	capillary number ( $\mu_L j/\sigma$ )	$\beta$	length fraction of Taylor-flow unit cell occupied by Taylor bubble
$c_p$	specific heat ( $\text{kJ kg}^{-1} \text{K}^{-1}$ )	$\delta_f$	liquid film thickness (m)
$D$	diameter (m)	$\Gamma$	drift flux parameter in bubble velocity model
$D_H$	hydraulic diameter (m)	$\Delta$	difference
$f_i$	body force vector ( $\text{kg m}^{-2} \text{s}^{-2}$ )	$\theta$	generic material property
$f$	Darcy friction factor, or blending factor	$\mu$	dynamic viscosity ( $\text{kg m}^{-1} \text{s}^{-1}$ )
$G$	mass flux ( $\text{kg m}^{-2} \text{s}^{-1}$ )	$\rho$	fluid density ( $\text{kg m}^{-3}$ )
$Gz$	Graetz number ( $D Re_j Pr_L/L_s$ )	$\sigma$	surface tension ( $\text{kg s}^{-2}$ )
$g$	gravitational acceleration ( $9.81 \text{ m s}^{-2}$ )	$\tau$	shear stress ( $\text{kg m}^{-1} \text{s}^{-2}$ )
$h$	convection heat transfer coefficient ( $\text{W m}^{-2} \text{K}^{-1}$ )	$\varphi$	volumetric flow rate through mesh cell faces ( $\text{m}^3 \text{s}^{-1}$ )
$H$	height (m)	<i>Subscripts</i>	
$i$	enthalpy ( $\text{kJ kg}^{-1}$ )	0	non-limited value
ID	inner diameter (m)	avg	average value
$j$	superficial velocity ( $\text{m s}^{-1}$ )	b	Taylor bubble (in Taylor-flow model)
$k$	thermal conductivity ( $\text{W m}^{-1} \text{K}^{-1}$ )	BPG	bubble pump generator
$L$	length (of liquid slug or Taylor bubble)	Ca	capillary scale
$L_b^*$	dimensionless bubble length ( $L_b/(Re_b D_b)$ )	CF	coupling fluid
$\dot{m}$	mass flow rate ( $\text{kg s}^{-1}$ )	d	dynamic component of pressure drop
$n$	number of mesh cells in a direction	DevSlug	model assuming developing flow in liquid slug
$\hat{n}$	cell-face normal	evap	evaporation
$N_f$	viscous force parameter ( $\sqrt{\rho_L(\rho_L - \rho_V)gD^3/\mu_L^2}$ )	f	cell-face value
$Nu$	Nusselt number ( $Nu = h D/k$ )	hs	hydrostatic forces
OD	outer diameter (m)	$i$	initial value, inner tube, cell or node index in discretized model
$p$	pressure (Pa)	in	inlet value
$p_{\rho gh}$	dynamic pressure (hydrostatic contribution removed) (Pa)	int	interface threshold value (in phase-change model), or interface position
$Pr$	Prandtl number ( $\mu c_p/k$ )	L	liquid phase
$Q$	heat transfer rate (W)	LO	value for all channel flow being liquid
$q$	heat flux ( $\text{W m}^{-2}$ )	LS	large diameter tube scale
$\dot{q}_{pc}$	Volumetric phase-change heat source ( $\text{kW kg}^{-1}$ )	LV	phase change (liquid-to-vapor)
$r$	radius (m)	LW	value from Liu and Winterton boiling model [47]
$R'$	thermal resistance $\times$ unit length ( $\text{m K W}^{-1}$ )	mod	model value
$R''$	thermal resistance $\times$ unit area ( $\text{m}^2 \text{K W}^{-1}$ )	o	outer tube
$Re_b$	Taylor bubble Reynolds number ( $\rho_V(U_B - U_{LF})D_B/\mu_V$ )	out	outlet value
$Re_{CF}$	coupling-fluid Reynolds number ( $\rho_{CF}U_{CF}D_{H,CF}/\mu_{CF}$ )	$r$	radial component
$Re_j$	superficial Reynolds number ( $\rho_L j D/\mu_L$ )	s	liquid slug (in Taylor-flow model)
$s$	under-relaxation factor	sat	saturated thermodynamic state
$t$	time (s)	seg	segment value in discretized model
$T$	temperature ( $^{\circ}\text{C}$ )	sim	simulation value
$T_0$	reference temperature ( $^{\circ}\text{C}$ )	trans	flow-transition pressure drop
$u$	velocity vector ( $\text{m s}^{-1}$ )	V	vapor phase
$u^*$	velocity field, corrected to prevent interface smearing ( $\text{m s}^{-1}$ )	wall	domain wall or inside wall of steam tube
$U$	phasic velocity ( $\text{m s}^{-1}$ )	WF	working fluid
$V$	volumetric flow rate ( $\text{m}^3 \text{s}^{-1}$ )	WK	value from model of Wadekar and Kenning [48]
$\dot{v}_{pc}$	volumetric dilatation rate due to phase change ( $\text{s}^{-1}$ )	$z$	axial component
$x$	mass flow quality		
$x_i$	position vector (m)		
$z$	axial position from bubble pump inlet (m)		

flows, it is possible to evaluate spatially varying quantities and individually assess BPG sub-models.

A number of mature approaches have been developed to simulate adiabatic two-phase flows, including Volume-of-Fluid (VOF) [7], level set [8], direct interface tracking [9], and two-fluid Eulerian-Eulerian formulations. However, techniques for simulating two-phase flows with phase-change heat transfer are still in their infancy. Phase-change formulations generally incorporate a

thermal-energy transport equation in addition to the governing flow equations, and apply appropriate phase-change source terms in the vicinity of liquid-vapor interfaces [10,11]. Such techniques can be applied to investigate developing two-phase flow phenomena in BPGs, enabling high fidelity assessment of incorporated sub-models. In the next section, reviews of prior work on distributed-heated BPGs and the most relevant phase-change flow simulation studies are presented.

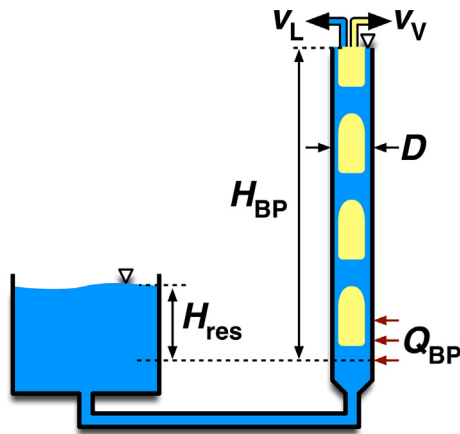


Fig. 1. Schematic of a spot-heated bubble-pump generator.

## 1.2. Prior work

### 1.2.1. Distributed-heated bubble-pump generator studies

In conventional BPGs, heat transfer occurs over a small area that is heated electrically or with a gas flame. This thermal input has been usually modeled as a step-change in flow conditions [12]. van der Walt [13] conducted a BPG modeling study, and incorporated flow-boiling heat transfer correlations to analyze the developing flow in the short generator region.

Koyfman et al. [14] performed experiments on an R-22 BPG. Input heat was supplied by a coupling-fluid (CF) stream flowing through a copper tube coiled around the BPG. The heat transfer area was relatively larger than in most spot-heated designs, but still only accounted for a small portion of the BPG surface.

Jakob et al. [4] developed a vertical shell-and-tube coupling-fluid-heated BPG for a residential-scale (2.5 kW cooling) DAR air-conditioning system. Their approach employed the full outside area of the BPG tubes for heat transfer, enabling operation with low source temperatures. Jakob et al. [4] described five design iterations, indicating the difficulty of designing a BPG to operate in this distributed heating mode. Detailed BPG models and performance results were not reported.

Dammak et al. [6] conducted a modeling study of an inclined full-length uniformly heated BPG that could be integrated into a flat-plate solar collector. Their BPG model was based on the approach of White [15]. Benhimidene et al. [16] also conducted a modeling study of a full-length uniformly heated BPG. Void fraction results were compared to those obtained with other models in the literature, but liquid pumping predictions were not assessed.

Rattner and Garimella [1] performed an experimental investigation of a tube-in-tube full-length CF-heated BPG with ambient-pressure steam-water working fluid. A segmented coupled-heat transfer and two-phase flow model was developed, and good agreement was found with experimental results for outlet liquid and vapor flow rates and overall heat transfer. However, predicted axial variation of quantities and submodel results could not be independently assessed (e.g., local flow rates, void fraction, hydrodynamic pressure drop, heat flux).

A more comprehensive review of BPG technologies and investigations can be found in [17].

### 1.2.2. Phase-change flow simulation studies

A number of Eulerian-Eulerian (*two-fluid*) simulation studies of flow-boiling [18,19] have been performed. These studies have primarily focused on large-diameter channels for nuclear reactors. Recently, similar approaches have been applied to distributed-heated BPGs. Garma et al. [20] performed an Eulerian-Eulerian simulation of BPG flow. Their study was conducted on a 2D

axisymmetric mesh geometry, and employed established interfacial transport and wall boiling models. Jo et al. [21] performed similar simulations of uniformly heated BPGs. Mesh independence was demonstrated, and results were compared with data from experimental studies and other flow-boiling simulations. Liquid pumping rate predictions were compared with those from the 1-D modeling study of Benhimidene et al. [16], and significant variations were found.

Such *two-fluid* approaches employ separate momentum equations for the liquid and vapor phases, and model interactions through subgrid-scale models (e.g., for the drag of small dispersed bubbles on the liquid bulk). It is unclear if such approaches can accurately represent the behavior of the anticipated Taylor flow pattern in BPGs, for which flow structures (e.g., elongated bubbles) are of similar scale to the full channel. *One-fluid* simulation techniques solve a single set of consistent governing equations, and may be more applicable. Most one-fluid phase-change simulation studies have focused on high resolution analysis of transport phenomena, such as nucleate boiling of individual or few bubbles [22,23], film boiling [24,25], or individual bubble condensation and mass transfer [26–28]. Fewer simulation studies of phase-change developing flow processes along full channels are available.

Mukherjee and Kandlikar [29] formulated a level-set based approach to simulate growth of a vapor bubble in a microchannel with flowing water. Qualitative agreement was found with experiments for bubble shape and wall-dryout. Yang et al. [30] performed VOF-based simulations and experimental investigations on flow boiling of R141b in a horizontal tube. They formulated an empirical rate-parameter based model to evaluate phase-change rates at the interface. They found local qualitative agreement of two-phase flow patterns between experimental and simulation results. Fang et al. [31] simulated boiling flows in a vapor venting microchannel, in which a semipermeable membrane permitted vapor removal to improve heat transfer performance and decrease frictional losses. Fang et al. [31] adopted the overall phase-change formulation of [30], but did not account for the volume generation due to evaporation. Overall, the success of these simulation studies indicates the feasibility of simulating flow-evaporation in distributed heated BPGs.

## 1.3. Present investigation

The objective of the present investigation is to analyze the developing heat transfer and two-phase flow in a tube-in-tube distributed CF-heated BPG. The configuration is based on that investigated experimentally in [1]. A special purpose VOF solver is implemented based on the open source interFoam code [32]. The condensation phase-change model of [10] is extended to address challenges specific to evaporation, and is incorporated into the solver. This solver is validated for film evaporation on a horizontal surface (Stefan problem). This formulation is then employed to perform 2-D axisymmetric simulations of a saturated-flow portion of the BPG, including both the inner- (working fluid) and CF-channels. Results are applied to assess heat transfer and two-phase flow predictions from the 1-D segmented BPG model of [1] with Taylor flow closure models of [33] (summarized in Appendix A). This approach enables rigorous evaluation of individual sub-models and axial parameter variations, which was not possible in prior experiments that only quantified global flow and heat transfer values.

## 2. Simulation approach and validation

### 2.1. Governing equations and overall formulation

The simulation formulation employed here is based on that developed in [10], which is an extension of the open source

adiabatic incompressible two-phase flow solver interFoam [32]. This solver follows the VOF formulation, in which a single set of governing equations is solved for both fluid phases (liquid and vapor). Local fluid material properties are determined by a weighted average of the phase fraction field ( $\alpha_1$ ), which is 0 in the vapor bulk, 1 in the liquid bulk, and ranges between these two limits in the vicinity of the interface.  $\alpha_1$  is advected by the solved velocity field, yielding consistency between the governing equations.

The incompressible continuity equation is modified with a source term ( $\dot{v}_{pc}$ ) representing the dilatation rate due to phase change. The compressible form of the continuity equation is not necessary because the densities of the liquid and vapor phases are assumed constant.

$$\frac{\partial u_i}{\partial x_i} = \dot{v}_{pc} \quad (1)$$

The momentum equation is formulated neglecting compressibility effects. Surface tension and gravitational forces are incorporated into a term  $f$ , following the interFoam formulation [34]. Surface tension forces are obtained without geometric reconstruction by estimating local curvature and interface orientation using differential operations on the phase field  $\alpha_1$  [35].

$$f_i = -\left(\frac{\partial \rho}{\partial x_i}\right) g_j x_j + \sigma \left\{ \frac{\partial}{\partial x_j} \left[ \frac{\partial \alpha_1}{\partial x_j} \right] / \left( \left( \frac{\partial \alpha_1}{\partial x_k} \frac{\partial \alpha_1}{\partial x_k} \right)^{1/2} \right) \right\} \frac{\partial \alpha_1}{\partial x_i} \quad (2)$$

Here,  $g$  is the gravitational acceleration vector, and  $\sigma$  is the fluid surface tension.

The complete momentum equation is formulated using  $p_{\text{pgh}}$  – the pressure field without the hydrostatic component:

$$\rho \frac{\partial u_i}{\partial t} + \rho u_j \frac{\partial u_i}{\partial x_j} - \mu \frac{\partial u_i}{\partial x_j \partial x_j} = -\frac{\partial p_{\text{pgh}}}{\partial x_i} + f_i \quad (3)$$

In the numerical implementation, the continuity constraint (Eq. (1)) is substituted into the momentum equation to yield a pressure correction equation.

$$\frac{\partial}{\partial x_i} \cdot \left( \frac{1}{A_D} \frac{\partial p_{\text{pgh}}}{\partial x_i} \right) = \nabla \cdot \phi - \dot{v}_{pc} \quad (4)$$

Following the approach of [36], the coefficients of the pressure equation are obtained from the diagonal entries of the momentum matrix equation ( $1/A_D$ ). Here,  $(\nabla \cdot \phi)$  is the numerical equivalent of the divergence of the velocity field ( $u_i$ ) for a cell. During each simulation time step, the solver iteratively corrects  $p$  and  $u$  using the Pressure Implicit with Splitting of Operators (PISO) [37] approach. In the OpenFOAM environment, PISO is repeated for multiple iterations at each time step using the merged PISO-SIMPLE or the PIMPLE process, where the Semi-Implicit Method for Pressure-Linked Equations (SIMPLE) is a classical iterative pressure-velocity solution algorithm for steady flows [38].

A thermal energy transport equation is employed to solve for the enthalpy ( $i$ ), in which viscous dissipation and pressure transport terms are assumed negligible compared to the large convective and conduction heat fluxes encountered during phase change. A volumetric heat source term  $\left( \frac{\partial i}{\partial t} + \frac{\partial}{\partial x_i} (u_i i) = \frac{\partial}{\partial x_i} \left( \frac{k}{\rho} \frac{\partial T}{\partial x_i} \right) - \dot{q}_{pc} \right)$  is included to account for the latent heat of phase-change.

During each simulation time step, the enthalpy field is first evaluated from the temperature field (here  $i(T) = c_p(T - T_0)$ ). Then, for a user-defined number of steps (typically 2–3), alternating corrections of the energy equation and update of the temperature field ( $T(i)$ ) are performed. This process is needed to solve iteratively for the temperature and enthalpy for fluids with non-constant specific heats. Alternating correction of the  $i$  and  $T$  fields leads to conver-

gence for both fields in a manner similar to the PIMPLE algorithm for  $u$  and  $p_{\text{pgh}}$ . The evaluated thermal energy equation incorporates an artificial enthalpy diffusion term to avoid solution “checkerboarding” [38].

Finally, the phase transport equation is formulated with a generation term to account for the change in liquid volume fraction due to phase change ( $\dot{\alpha}_{1,pc}$ ). Here, the velocity field ( $u$ ) is modified with a compressive term in the vicinity of liquid–vapor interfaces to counteract numerical diffusion of  $\alpha_1$ , yielding  $u^*$  [34].

$$\frac{\partial \alpha_1}{\partial t} + \frac{\partial}{\partial x_i} (u_i^* \alpha_1) = \dot{\alpha}_{1,pc} \quad (6)$$

Material properties are evaluated for each mesh cell. Surface tension ( $\sigma$ ) and the phase-change enthalpy ( $i_{LV}$ ) are assumed uniform. The fluid density ( $\rho$ ), viscosity ( $\mu$ ), and thermal conductivity ( $k$ ) are defined to be the volume-fraction weighted average of the liquid and vapor phase values:

$$\theta = \alpha_1 \theta_L + (1 - \alpha_1) \theta_V \quad \theta \in [\rho, \mu, k] \quad (7)$$

The specific heat of the fluid ( $c_p$ ) is evaluated using a mass-weighted average for each mesh cell:

$$c_p = \frac{\alpha_1 \rho_L c_{p,L} + (1 - \alpha_1) \rho_V c_{p,V}}{\rho} \quad (8)$$

Liquid and vapor specific heats are assumed constant in the present investigation; therefore, the fluid enthalpy can be related to temperature as:

$$i = c_p(T - T_{\text{sat}}) \quad (9)$$

The enthalpy of phase change is not included in the above expression because it is accounted for in  $\dot{q}_{pc}$ .

Simulation closure is obtained by coupling the governing equations (Eqs. (3)–(6)) and constitutive relations (Eqs. (7)–(9)) with a phase-change model, described in the following section.

## 2.2. Phase-change model formulation

The phase-change model implemented here operates using readily available volumetric field data, rather than employing interfacial area density and interfacial temperature gradients as in the formulations of [25,39,40]. As such, complex and potentially computationally expensive geometric interface reconstruction from the volume-fraction field ( $\alpha_1$ ) is avoided. The predicted rate of phase change is linked to the simulation time-step size ( $\Delta t$ ), rather than empirical rate parameters as in the approaches of [30,31,41]. Thus, the resulting formulation can yield mesh-independent results for general phase-change problems without interface reconstruction.

First, a scan is performed over all mesh cell faces to identify neighboring cell pairs that contain the interface. These pairs are identified as those for which the cell values of  $\alpha_1$  straddle a user-specified interface value ( $\alpha_{\text{int}} = 0.5$  in [10]) (Fig. 2). This approach results in a finite interface thickness (i.e., two-cell widths). However, as mesh resolution increases, the interface thickness converges to 0. In the condensation-specific study of [10], mesh wall cells were also included in the interface-containing set, permitting film condensation on dry walls.

Next, an initial non-limited volumetric phase-change heat source is evaluated for interface cells:

$$\dot{q}_{pc,0} = \frac{\rho c_p (T - T_{\text{sat}})}{\Delta t} \quad (10)$$

This phase-change model does not account for the internal thermal resistance in interface cells. However, the interface-cell contributions to overall thermal resistance are generally negligible in a two-phase flow simulation, provided that the mesh resolution is



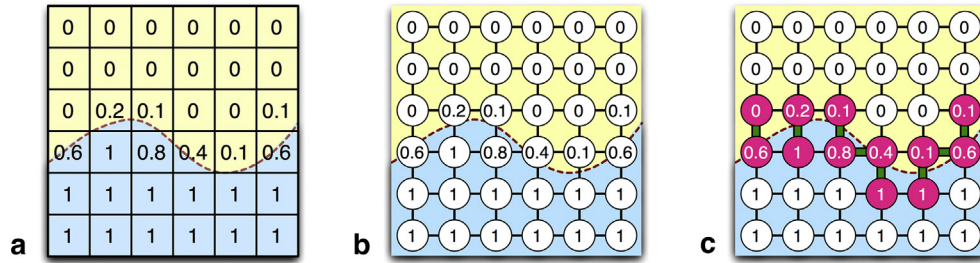


Fig. 2. Interface cell identification process: The phase fraction field on mesh cells (a) yields a graph (b) from which cell pairs straddling  $\alpha_{1,\text{int}} = 0.5$  form the interface (c).

sufficient. For example, for a case of evaporation of a liquid film resolved with 50 uniform mesh cells, this approach would under-predict the overall thermal resistance by at most  $\sim 2\%$  (corresponding to the cell with the major portion of phase-change in the two-cell thick interface region). If the mesh is refined near the interface, this error can be further reduced.

$\dot{q}_{\text{pc},0}$  is then limited to ensure that the phase-change rate does not violate the fluid availability constraint (e.g., condensing more vapor than is available in a cell per time step). This limiting condition would be necessary, for example, if a small amount of vapor flowed into a highly subcooled liquid cell. If the unlimited phase-change rate result were applied (Eq. (10)), the cell temperature would be forced to  $T_{\text{sat}}$ , even if the equilibrium state should still be that of subcooled liquid. A second limiting condition is applied for  $\dot{q}_{\text{pc},0}$  to ensure that the CFL condition is satisfied (i.e., that the velocity change due to phase change does not exceed  $\Delta x/\Delta t$ ). Additional details of the phase-change limiting algorithm are reported in [10].

Once  $\dot{q}_{\text{pc}}$  is obtained for interface cells, the dilatation ( $\dot{v}_{\text{pc}}$ ) and phase fraction generation ( $\dot{\alpha}_{1,\text{pc}}$ ) source terms are evaluated:

$$\dot{v}_{\text{pc}} = \frac{\dot{q}_{\text{pc}}}{i_{\text{LV}}} \left( \frac{1}{\rho_{\text{V}}} - \frac{1}{\rho_{\text{L}}} \right) \quad (11)$$

$$\dot{\alpha}_{1,\text{pc}} = -\frac{\dot{q}_{\text{pc}}}{\rho i_{\text{LV}}} \quad (12)$$

This phase-change formulation was previously validated for horizontal film condensation (Stefan problem), smooth falling-film condensation (Nusselt problem), and wavy falling-film condensation [10]. Convergence to grid-independent results was also demonstrated with increasing mesh resolution. In the following section, this phase-change formulation is extended to enable support of evaporation phenomena for the distributed-heated BPG application.

### 2.3. Evaporative phase-change model

The formulated governing equations and analytical phase-change source term definitions are equally valid for the cases of condensation and evaporation. However, the nature of evaporation necessitates different implementation and numerical techniques for multiple reasons:

1. From a thermodynamic perspective, the fluid phases in condensation on a surface are in equilibrium states (subcooled liquid and saturated vapor). However, the liquid in film evaporation on a surface is superheated. In practice, liquid film evaporation transitions to boiling under certain conditions. Thus, an evaporation model must incorporate logic to suppress or model boiling.

2. Condensation is a numerically stable process in VOF simulations because it effects a volumetric sink on the interface. This yields compressive velocity currents that counteract numerical diffusion of the interface. In contrast, the volumetric source ( $\dot{v}_{\text{pc}}$ ) generated during evaporation acts to spread the interface, and places an additional burden on interface compression schemes. Additionally, this volumetric source can cause false liquid production due to the diffuse nature of the interface.
3. Film condensation on a surface is a physically stable process. For example, over-condensation in one time step will yield an overly-thick liquid film with increased heat transfer resistance, reducing the condensation rate in future time steps. In contrast, over-evaporation initiates a compounding process in which the film thickness and heat transfer resistance successively decrease, leading to “runaway” evaporation and dryout.

The phase-change model presented in the previous section is modified to address these challenges of evaporation phenomena. First, the phase-change heating term is set to 0 for super-heated non-interface-containing wall-cells. This suppresses evaporation at the liquid-wall interface. Evaporation can still occur at the liquid-vapor interfaces of bubbles attached to heated walls, which is the underlying mechanism of nucleate boiling. However, this approach does not permit the spontaneous formation of vapor bubbles on a completely wetted surface.

The second challenge (interface-spreading) is addressed with two modifications to the phase-change model. First, different interface identification threshold values ( $\alpha_{1,\text{int}}$ ) are employed for condensation and evaporation. Here  $\alpha_{1,\text{int}} = 0.9$  is employed for condensation ( $T < T_{\text{sat}}$ ) and  $\alpha_{1,\text{int}} = 0.1$  for evaporation ( $T > T_{\text{sat}}$ ). This approach applies the evaporation source terms on the “vapor side” of the interface. Thus, the dilatation rate source ( $\dot{v}_{\text{pc}}$ ) from evaporation will transport less and generate less liquid because the advective phase-fraction flux on vapor-side cell faces,  $(u\alpha_1)_f$ , will be small.

Second, a phase-change volume source splitting operation is applied, similar to the approach of [42]. In this process, the vapor-phase portion of  $\dot{v}_{\text{pc}}$  ( $\dot{q}_{\text{pc}}/(i_{\text{LV}}\rho_{\text{V}})$ ) is shifted away from interface cells to the vapor region (down the gradient of  $\alpha_1$ ). Similarly, the liquid-phase portion of  $\dot{v}_{\text{pc}}$  ( $-\dot{q}_{\text{pc}}/(i_{\text{LV}}\rho_{\text{L}})$ ) is shifted into the liquid region.  $\dot{v}_{\text{pc}}$  is transferred from each interface cell to neighboring cells with distribution weighted by the relative dot product of the gradient of the phase-fraction field and cell-face area normal vectors  $((\partial\alpha_1/\partial x_i)A_{f,i})$ . This process is applied in multiple passes (4) to ensure that potential  $\dot{v}_{\text{pc}}$  transfer between neighboring interface cells is almost entirely shifted to the vapor and liquid bulk regions. This algorithm is illustrated schematically in Fig. 3. These two modifications to the phase-change model lead to slightly increased effective interface thickness. However, the overall algorithm still recovers the governing continuum scale phenomena, provided that the mesh is sufficiently resolved in the vicinity of the interface.

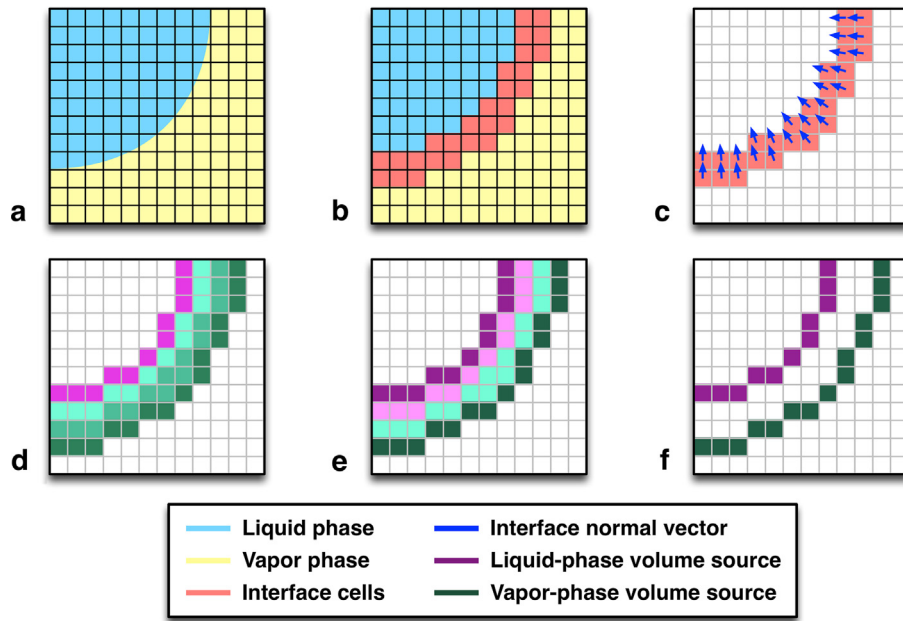


**Fig. 3.** Schematic of dilatation rate source ( $\dot{v}_{pc}$ ) splitting and shifting process. (a) Liquid-vapor interface profile, (b) Interface-cell identification, (c) Interface normal vector field, (d–f) Progressive shifting of liquid and vapor phase-change volume sources away from interface.

1. Initialize simulation data and phase change model
2. **WHILE**  $t < t_{end}$  **DO**
  1. Update  $\Delta t$  for stability
  2. Update fluid properties
  3. Update phase change model ( $\dot{q}_{pc}$ ,  $\dot{v}_{pc}$ ,  $\dot{\alpha}_{pc}$ )
  4. Phase equation sub-cycle
  5. **DO** PIMPLE
    1. Form  $u$  equation
    2. PISO
      1. Obtain and correct face fluxes ( $\phi$ )
      2. Solve  $p$ -Poisson equation
      3. Correct  $u$
6. **LOOP**
7. Update  $i(T)$
8. **DO** Energy Loop
  1. Solve  $i$  equation
  2. Update  $T(i)$
9. **LOOP**
3. **LOOP**

**Fig. 4.** Summary of phase-change flow solver algorithm.

The third challenge of “runaway” evaporation is more fundamental. The physical counterpart (film dryout) to the numerical problem is a major safety concern in many thermal energy systems. This issue can only be addressed by reducing numerical discretization error. In the present investigation, fine meshes and small integration time steps are employed to limit error accumulation. Higher order discretization and integration schemes could also be employed in future studies.

The complete phase-change flow simulation algorithm is summarized in Fig. 4. In the following section, this formulation is assessed for the problem of horizontal film evaporation (Stefan problem) (see Fig. 5).

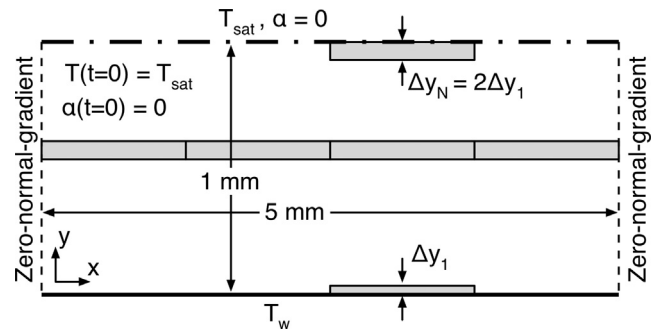


**Fig. 5.** Geometry for horizontal film evaporation studies.

## 2.4. Evaporative phase-change model assessment

The proposed phase-change model is applied to horizontal liquid film evaporation on a heated surface. The problem configuration considered here matches that employed to assess the condensation phase-change model in [10]. The working fluid properties are those of saturated isobutane at 25 °C. A 2D rectangular domain is employed with horizontal and vertical dimensions of 5.0 mm and 1.0 mm, respectively ( $0 \leq x \leq 5\text{ mm}$ ,  $0 \leq y \leq 1\text{ mm}$ ). The mesh is defined with four uniform cells per horizontal row, and 200 in the vertical direction. The mesh is uniformly graded in the vertical direction, with cells in the bottom row being half the height of the uppermost row. Zero-normal-gradient boundary conditions are applied to the vertical sides of the domain (i.e.,  $\nabla \theta \cdot \hat{n} = 0$ , or equivalently,  $\partial \theta / \partial x = 0$  for all solved fields  $\theta$ ). Thus, the domain represents a section of an infinitely wide evaporating film. The bottom wall is set to  $T_{wall} = 30^\circ\text{C}$ , and the top “freestream” boundary is set to the saturation temperature:  $T_{sat} = 25^\circ\text{C}$ . All fluid flowing through the freestream boundary is vapor ( $\alpha_1 = 0$ ). A schematic of the simulation domain is presented in Fig. 6. The liquid film is set to an initial thickness of  $\delta_i = 0.201\text{ mm}$  with a linear temperature profile from  $T_{wall}$  to  $T_{sat}$  in the film. The exact analytical solution for developing film thickness is:

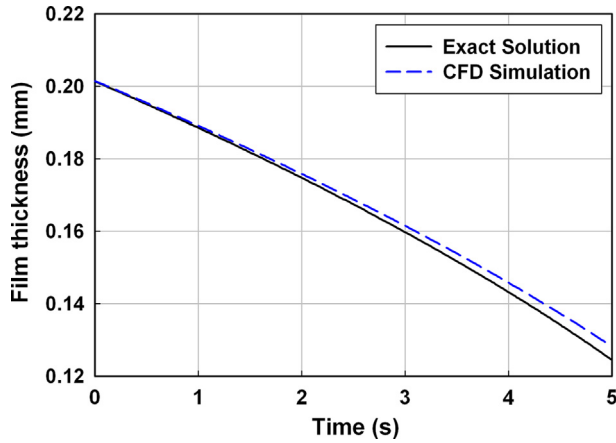


Fig. 6. Development of simulated evaporating horizontal film thickness.

Table 1

Representative phase-fraction field ( $\alpha_1$ ) values in cells near the interface for corresponding condensation and evaporation simulations.

Condensation	Evaporation
1	0.9999980
1	0.9993100
1	0.9470470
0.971934	0.4134600
0	0.0103317
0	0.0001184
0	0.0000155

$$\delta_{\text{mod}}(t) = \left[ \delta_i^2 + 2t \left( \frac{k}{\rho c_p} \right)_L \left( \frac{1}{2} - \frac{i_{LV}}{c_{p,L} \Delta T} \right)^{-1} \right]^{1/2} \quad (13)$$

Analytical model and simulation results for the evaporating film thickness are presented in Fig. 6. Relative errors in evaporated film thickness ( $|\delta_{\text{sim}} - \delta_{\text{mod}}|/(\delta_i - \delta_{\text{mod}})$ ) reach 4.8% after 5 simulation seconds (about 40% evaporation of liquid film). This error is relatively small, but is still significantly greater than was found for a comparable condensation case with the same mesh resolution (0.6% error) in [10].

Representative interface-region phase-fraction ( $\alpha_1$ ) profiles for the horizontal film condensation and evaporation cases are presented in Table 1. Due to the compressive nature of condensation phase change ( $\dot{v}_{pc} < 0$ ), the interface is only three cells thick. In

contrast, evaporation causes interface spreading, requiring a thickness of five cells for the transition from  $\alpha_1 < 0.001$  to  $\alpha_1 > 0.999$ . Overall, this analysis demonstrates that the proposed modifications to the phase-change model are acceptable for evaporation simulations. However, care must be taken to limit discretization error and ensure sufficiently resolved interface regions.

### 3. Simulation of distributed-heated bubble-pump generator

#### 3.1. Simulation setup

A simulation study is performed for a co-flow tube-in-tube BPG with evaporating working fluid flow in the inner tube ( $ID_i = 7.8$  mm), and heating coupling-fluid (CF) flow in the annulus ( $OD_i = 9.5$  mm,  $ID_o = 10.9$  mm) (Fig. 7). As in Section 2.4, both the flow equations (for  $u, p, \alpha_1$ ) and thermal energy transport equation (for  $i$  and  $T$ ) are solved simultaneously, and are coupled through the phase-change model (Sections 2.2–2.3). In this study, the working fluid transport properties are relaxed compared with the ambient-pressure steam-water flows investigated in [1] (increased  $\mu_L$ , increased  $\rho_V/\rho_L$ ). This improves numerical stability and decreases the required mesh resolution while still allowing assessment of the segmented BPG model (summarized in Appendix A). The specified enthalpy of vaporization is correspondingly reduced ( $i_{LV} = 200$  kJ kg<sup>-1</sup>) so that the vapor-volume production per unit of heat input ( $(\rho_V i_{LV})^{-1} = 2.5 \cdot 10^{-4}$  m<sup>3</sup> kJ<sup>-1</sup>) is of similar order to values in BPGs operating with steam or ammonia with lower  $\rho_V$  values (for ammonia at 50 °C  $(\rho_V i_{LV})^{-1} = 6.0 \cdot 10^{-5}$  m<sup>3</sup> kJ<sup>-1</sup>; for water at 100 °C  $(\rho_V i_{LV})^{-1} = 7.4 \cdot 10^{-4}$  m<sup>3</sup> kJ<sup>-1</sup>). CF properties are representative of a mineral-oil based heat transfer fluid. Fluid properties are summarized in Table 2. Properties of ambient-pressure steam-water are also reported for reference.

The studied case focuses on an  $L = 0.30$ -m-long section of the saturated flow portion of a BPG. In the simulation results, this domain contains 8.2 Taylor bubble-liquid slug unit cells on average (average unit cell length 37 mm). Liquid and vapor inlet flow rates into this portion of the domain are  $V_{L,\text{in}} = 100$  ml min<sup>-1</sup> and  $V_{V,\text{in}} = 400$  ml min<sup>-1</sup> (total mass flux  $G = 37.7$  kg m<sup>-2</sup> s<sup>-1</sup>; phasic mass fluxes  $G_{V,\text{in}} = 2.8$  kg m<sup>-2</sup> s<sup>-1</sup>,  $G_{L,\text{in}} = 34.9$  kg m<sup>-2</sup> s<sup>-1</sup>). The CF flow enters the domain at  $V_{CF} = 200$  ml min<sup>-1</sup> and  $T_{CF,\text{in}} - T_{\text{sat}} = 10$  K. For these conditions, the segmented model predicts a liquid outlet flow rate of  $V_{L,\text{out}} = 95$  ml min<sup>-1</sup> ( $G_{L,\text{out}} = 33.1$  kg m<sup>-2</sup> s<sup>-1</sup>), vapor outlet flow rate of  $V_{V,\text{out}} = 635$  ml min<sup>-1</sup> ( $G_{V,\text{out}} = 4.4$  kg m<sup>-2</sup> s<sup>-1</sup>), and total heat transfer rate of  $Q = 15.7$  W. Inlet and outlet conditions predicted by the segmented model for this part of the saturated flow

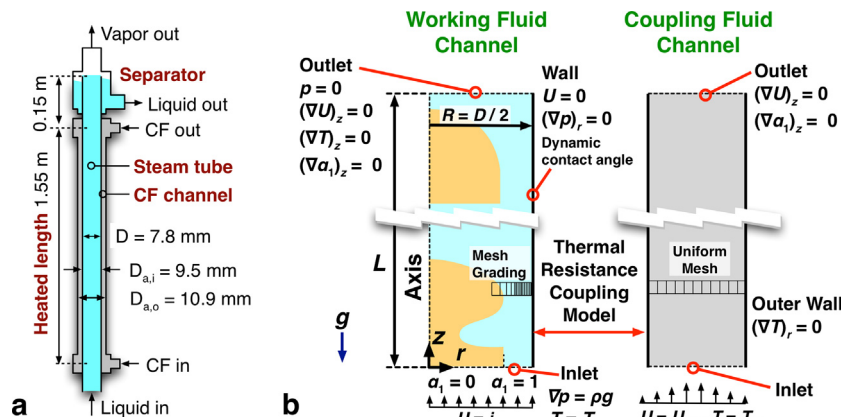


Fig. 7. (a) Coupling-fluid heated bubble-pump generator geometry, (b) Schematic of 2D axisymmetric simulation domain (coaxial working-fluid and coupling-fluid subdomains).

**Table 2**

Working fluid and coupling fluid properties for the distributed heated flow boiling experiments. Properties of ambient-pressure saturated steam-water are included for reference (as employed in [1]).

Property	Liquid phase	Vapor phase
<b>Working fluid</b>		
Density ( $\text{kg m}^{-3}$ )	1000	20
Dynamic viscosity ( $\text{kg m}^{-1} \text{s}^{-1}$ )	$3 \times 10^{-3}$	$3 \times 10^{-4}$
Specific heat ( $\text{kJ kg}^{-1} \text{K}^{-1}$ )	2.0	1.5
Thermal conductivity ( $\text{W m}^{-1} \text{K}^{-1}$ )	0.5	0.05
Surface tension ( $\text{kg s}^{-2}$ )	0.04	
Enthalpy of phase change ( $\text{kJ kg}^{-1}$ )	200	
<b>Ambient Pressure Saturated Steam-Water (<math>T = 100^\circ\text{C}</math>, <math>p = 1 \text{ atm}</math>, included for reference)</b>		
Density ( $\text{kg m}^{-3}$ )	959	0.6
Dynamic viscosity ( $\text{kg m}^{-1} \text{s}^{-1}$ )	$2.8 \times 10^{-4}$	$1.2 \times 10^{-5}$
Specific heat ( $\text{kJ kg}^{-1} \text{K}^{-1}$ )	4.2	2.1
Thermal conductivity ( $\text{W m}^{-1} \text{K}^{-1}$ )	0.68	0.03
Surface tension ( $\text{kg s}^{-2}$ )	0.059	
Enthalpy of phase change ( $\text{kJ kg}^{-1}$ )	2259	
<b>Coupling fluid</b>		
Density ( $\text{kg m}^{-3}$ )		800
Dynamic viscosity ( $\text{kg m}^{-1} \text{s}^{-1}$ )		$5 \times 10^{-3}$
Specific heat ( $\text{kJ kg}^{-1} \text{K}^{-1}$ )		2000
Thermal conductivity ( $\text{W m}^{-1} \text{K}^{-1}$ )		0.1

**Table 3**

Inlet conditions and segmented model predicted outlet conditions for simulation saturated flow boiling domain.

Parameter		Inlet Value	Outlet Value (Predicted)	
Liquid flow rate	$V_L$	100.0	95.3	$\text{ml min}^{-1}$
	$G_L$	34.9	33.1	$\text{kg m}^{-2} \text{s}^{-1}$
Vapor flow rate	$V_V$	400.0	635.1	$\text{ml min}^{-1}$
	$G_V$	2.8	4.4	$\text{kg m}^{-2} \text{s}^{-1}$
Coupling fluid temperature	$T_{CF} - T_{\text{sat}}$	10.0	7.1	K
Coupling fluid flow rate	$V_{CF}$	200.0	200.0	$\text{ml min}^{-1}$

boiling section are summarized in Table 3. The simulation conditions can be summarized in terms of the main governing parameters: superficial-velocity Reynolds number  $Re_j = \rho_L j D_i / \mu_L = 460 - 660$ , liquid Prandtl number  $Pr_L = 12$ , Bond number  $Bo = (\rho_L - \rho_G) g D_i^2 / \sigma = 14$ ,  $N_f = \sqrt{\rho_L (\rho_L - \rho_G) g D_i^3 / \mu_L^2} = 710$ , and volumetric flow quality  $(V_V / (V_V + V_L)) = 0.8 - 0.9$ .

The simulation domain is presented schematically in Fig. 7b, and includes coupled 2-D axisymmetric sub-domains for the working fluid and CF channels. The working fluid mesh is refined near the wall ( $\Delta r = 0.031 \text{ mm}$  for  $2.88 \leq r \leq 3.88 \text{ mm}$ , 32 cells thick). This fine mesh region (1.0 mm thick) resolves the anticipated thin films around Taylor bubbles ( $\delta_f \sim 0.6 \text{ mm}$ ) with about 19 cells, exceeding the criterion of 5 cells suggested in [43]. An additional 45 cells extend from  $r = 0 - 2.88 \text{ mm}$ , and are graded such that the ratio of neighboring cell widths is 1.03 (i.e., matching the film-region mesh resolution at  $r = 2.88 \text{ mm}$ ). The mesh contains 4296 equal-height cells in the axial direction ( $\Delta z = 0.10 \text{ mm}$ ). The CF channel is meshed with 28 uniform-width cells in the radial direction ( $\Delta r = 0.025 \text{ mm}$ ), and 4296 cells in the axial direction (matching the working fluid channel). The inner stainless-steel tube wall is not resolved in detail, but rather is modeled as a thermal resistance between the two sub-domains ( $R''_{\text{wall}} = 6.9 \times 10^{-5} \text{ m}^2 \text{K W}^{-1}$  based on the outer surface area). Two coarser mesh simulations are also performed to assess grid sensitivity (see Section 3.2).

The inner channel is simulated following the overall formulation presented in Section 2. This approach does not account for

nucleate boiling on the wall; therefore, all phase change proceeds as convective flow evaporation. This assumption is reasonable because the predicted wall superheat is relatively low ( $T_{\text{wall}} - T_{\text{sat}} = 2.7 - 4.1 \text{ K}$  along the channel length). Reported wall superheats required for the onset of nucleate boiling often exceed 10 K [44], but specific values depend on surface properties, working fluids, and operating conditions.

The fluid inlet at the bottom of the working fluid domain is alternated between annular flow (vapor core, liquid annulus,  $R_{\text{int}} = 3.75 \text{ mm}$ , 85% of the time, period 0.077 s) and all liquid flow (15% of the time) at  $u_z = 0.177 \text{ m s}^{-1}$  and  $T = T_{\text{sat}}$ . This produces inlet bubbles of length  $\sim 1.5D$ , which is representative of the Taylor flow pattern that is expected to enter this portion of the BPG.

The inlet pressure is specified with a hydrostatic boundary condition ( $\partial p / \partial z = \rho g$ ). The top of the domain (outlet) is modeled as an outflow boundary, with zero normal-gradient conditions for  $\alpha_i$ ,  $u$ , and  $T$ . The outlet pressure is specified to be 0 (ambient pressure). The wall is modeled as a no-slip surface for the velocity field ( $u = 0$ ), and a zero-normal-gradient boundary for pressure. The dynamic wall contact-angle boundary condition is specified using the model of [45] as implemented by [46]. In general, the wall is expected to be wetted by liquid film, and this boundary condition model ensures that rewetting occurs after dryout events (not guaranteed for static contact angle models).

The wall temperature is modeled with an explicit coupling condition between the two domains. At the end of each simulation time step, the following conditions are applied for each working-fluid and CF wall cell-face-pair  $i$ .

$$\left( \frac{\partial T_{\text{CF,wall}}}{\partial r} \right)_i \leftarrow (1-s) \left( \frac{\partial T_{\text{CF,wall}}}{\partial r} \right)_i + s \frac{T_{\text{CF,wall},i} - T_{\text{wall},i}}{R''_{\text{wall}} k_{\text{CF}}} \quad (14)$$

$$\left( \frac{\partial T_{\text{wall}}}{\partial r} \right)_i \leftarrow - \left( \frac{\partial T_{\text{CF,wall}}}{\partial r} \right)_i \frac{k_{\text{CF}}}{k_{\text{wall},i}} \frac{OD_i}{ID_i} \quad (15)$$

Here,  $s$  is an under-relaxation factor employed to ensure simulation stability ( $s = 0.1$ ).  $T_{\text{CF,wall}}$  and  $T_{\text{wall}}$  are the wall surface temperatures in the CF and working fluid domains, respectively.  $k_{\text{wall}}$  is the working fluid thermal conductivity at the wall (generally  $k_{\text{wall}} = k_L$ ).

The velocity profile in the CF sub-domain is specified to be that of fully-developed laminar annular channel flow ( $Re_{\text{CF}} = 33$ ). The governing thermal energy transport equation for the sub-domain is:

$$\frac{\partial T_{\text{CF}}}{\partial t} + u_i \frac{\partial T_{\text{CF}}}{\partial x_i} = \frac{\partial}{\partial x_i} \left[ \left( \frac{k}{\rho c_p} \right)_{\text{CF}} \frac{\partial T_{\text{CF}}}{\partial x_i} \right] \quad (16)$$

Eq. (16) is solved during each simulation time step after stage 2.9 in the solver algorithm (Fig. 4), and before updating the wall heat-transfer coupling condition (Eqs. (14) and (15)). The temperature inlet to the CF domain is specified as that of laminar hydrodynamically and thermally fully developed annular flow with an insulated outer wall, an assumed wall conduction resistance of  $R''_{\text{wall}} = 6.9 \times 10^{-5} \text{ m}^2 \text{K W}^{-1}$ , and flow-evaporation convection coefficient of  $h_{\text{evap}} = 1000 \text{ W m}^{-2} \text{K}^{-1}$ . The sub-domain top surface (outlet) is modeled as a zero-normal-gradient temperature boundary. The outer wall is assumed adiabatic ( $\partial T / \partial r = 0$ ), and the inner wall temperature boundary condition is coupled to that of the working fluid, as described above.

The simulation is initialized for 2 ss. Simulation output data are then collected for 4 ss ( $U_b t / L \sim 5$ ), with checkpoint logging every 0.2 ss.



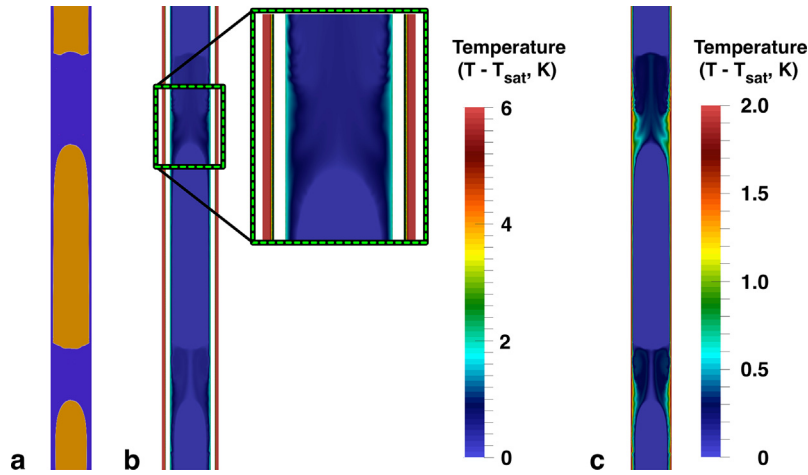


**Fig. 8.** Representative flow-boiling simulation two-phase flow pattern. (a) Working fluid phase distribution, (b) Working fluid and coupling fluid temperature profiles with zoom-in of bubble-nose region, (c) Detail view of working fluid temperature distribution.

**Table 4**

Inlet conditions and segmented model predicted outlet conditions for simulation saturated flow boiling domain. Relative deviations from baseline mesh results indicated in parentheses.

Parameter	Coarser Mesh (40 × 2160, 15 × 2160)	Coarse Mesh (55 × 3072, 20 × 3072)	Baseline Mesh (77 × 4296, 28 × 4296)
Heat transfer ( $Q_{BPG}$ , W)	18.96 (+3.8%)	18.57 (+1.7%)	18.26
Outlet vapor flow rate ( $V_{V,out}$ , ml min <sup>-1</sup> )	685.5 (+3.7%)	684.1 (+3.5%)	661.2
Vapor phase rise velocity ( $U_b$ , m s <sup>-1</sup> )	0.446 (+13.2%)	0.383 (-2.8%)	0.394
Void fraction ( $\alpha$ )	0.489 (-2.4%)	0.510 (+1.8%)	0.501
Dynamic axial pressure gradient ( $\nabla p_{d,z}$ , Pa m <sup>-1</sup> )	-778 (-24.8%)	-1015 (-1.9%)	-1035
Total axial pressure gradient ( $\nabla p_z$ , Pa m <sup>-1</sup> )	4331 (+9.4%)	3892 (-1.7%)	3959

### 3.2. Overall simulation assessment

The simulation progressed in a stable fashion. The evaporating phase-change model refinements (Section 2.3) ensured that liquid-vapor interface sharpness was maintained. The working-fluid channel flow was generally in the Taylor flow regime (Fig. 8a), although bubble interface profiles were occasionally distorted. Representative temperature profiles in the working fluid and coupling fluid channels are presented in Fig. 8b and c. Vapor-bulk temperatures were generally within 0.01 K of  $T_{sat}$ . Average wall  $y^+$  values were 0.25 (peak 3.2), indicating that the mesh is well resolved in the near-wall region.

Time-averaged volume and energy balances were performed over the working-fluid domain to assess conservation during the simulation. Average liquid and vapor flow rates were measured to be  $V_{L,in} = 99.5$  ml min<sup>-1</sup> ( $G_{L,in} = 34.7$  kg m<sup>-2</sup> s<sup>-1</sup>) and  $V_{V,in} = 399.8$  ml min<sup>-1</sup> ( $G_{V,in} = 2.8$  kg m<sup>-2</sup> s<sup>-1</sup>), respectively. Phase-change heating resulted in 261.7 ml min<sup>-1</sup> of volume generation. Averaged outlet flow rates were evaluated to be  $V_{L,out} = 99.8$  ml min<sup>-1</sup> ( $G_{L,out} = 34.8$  kg m<sup>-2</sup> s<sup>-1</sup>) and  $V_{V,out} = 661.2$  ml min<sup>-1</sup> ( $G_{V,out} = 4.6$  kg m<sup>-2</sup> s<sup>-1</sup>). Net volume conservation was thus achieved to within 0.008 ml min<sup>-1</sup>. However, a small amount of numerical liquid production occurred (5.6 ml min<sup>-1</sup>) due to the phase-change dilatation source term ( $\dot{v}_{pc}$ ), as discussed in Section 2.3.

Of the 18.26 W time-average heat transfer rate to the working fluid through the channel wall, 17.78 W resulted in evaporative

phase change, and 0.43 W was removed via the superheated liquid outlet flow. This sensible heating can occur, even for the saturated inlet conditions, because the liquid film and liquid slug regions are slightly superheated (up to ~2 K in this study). The remaining 0.05 W resulted in sensible thermal storage in the domain from the assumed initial condition ( $T(t = 0) = T_{sat}$ ), and decays to 0 W as the simulation time increases.

A mesh sensitivity study was performed with the baseline grid (working fluid channel:  $n_r \times n_z = 77 \times 4296$ , CF channel:  $n_r \times n_z = 28 \times 4296$ ) and two coarser grids (working fluid channel:  $n_r \times n_z = 55 \times 3072$  and  $40 \times 2160$ , CF channel:  $n_r \times n_z = 20 \times 3072$  and  $15 \times 2160$ ). Time- and volume averaged simulation results are summarized in Table 4. Most directly measured quantities ( $Q_{BPG}$ ,  $V_{V,out}$ ,  $\alpha$ ) deviate by less than 4% between all three cases. The coarser mesh simulation yielded somewhat distorted bubble profiles, which resulted in relatively high bubble rise velocities and decreased hydrodynamic pressure recovery. These quantities agree to within 3% between the coarse and baseline meshes. Similarly, the total axial pressure gradient ( $\nabla p_z = (\alpha\rho_V + (1 - \alpha)\rho_L)g + \nabla p_d$ ) agrees to within 2% for these higher resolution cases. Overall, this analysis indicates that relatively mesh independent results are obtained with the baseline mesh.

### 3.3. Heat transfer analysis

CF and smoothed inner wall temperatures are compared between time-averaged simulation results and segmented model

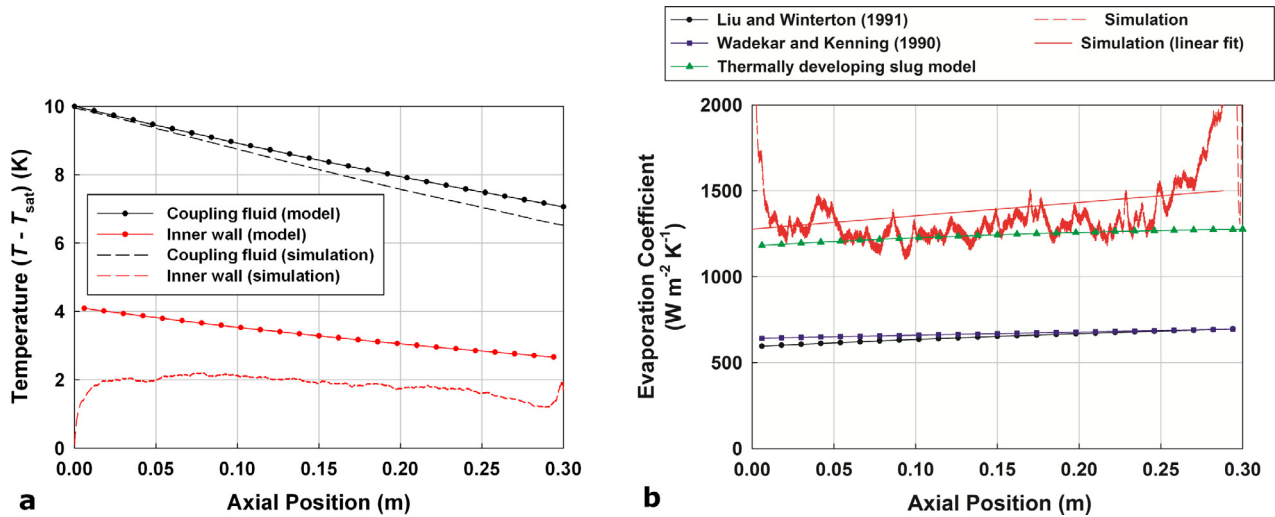


Fig. 9. Comparison of model and simulation profiles of (a) coupling fluid and inner-channel inner-wall temperatures and (b) convective flow evaporation heat transfer coefficient.

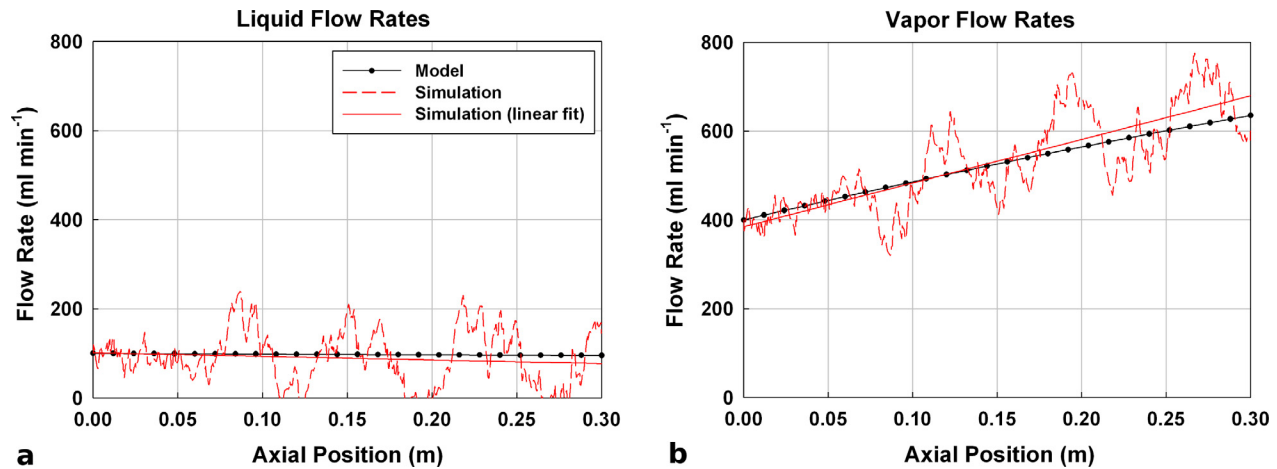


Fig. 10. Comparison of model and simulation profiles of (a) liquid and (b) vapor axial flow rates.

predictions in Fig. 9a. The CF temperature decreases by 18.1% more over the length of the domain in the simulation case ( $T_{\text{CF,sim}} = 10.0 \rightarrow 6.5 \text{ K}$ ,  $Q_{\text{BPG}} = 18.3 \text{ W}$ ) than in the segmented model ( $T_{\text{CF}} = 10.0 \rightarrow 7.1 \text{ K}$ ,  $Q_{\text{BPG}} = 15.7 \text{ W}$ ). This discrepancy is primarily due to the greater evaporative heat transfer coefficient obtained in the simulation ( $h_{\text{evap,avg}} = 1390 \text{ W m}^{-2} \text{K}^{-1}$ ) than with the flow evaporation model of [47] ( $h_{\text{evap,avg}} = 650 \text{ W m}^{-2} \text{K}^{-1}$ ) employed in the segmented model. This increased heat transfer coefficient can be inferred from the lower simulation wall temperature in Fig. 9a ( $T_{\text{wall,avg,sim}} = 1.84 \text{ K}$ ,  $T_{\text{wall,avg,mod}} = 3.32 \text{ K}$ ), and is presented directly in Fig. 9b. CF channel convection heat transfer coefficients agree closely between simulation ( $h_{\text{CF,sim}} = 332 \text{ W m}^{-2} \text{K}^{-1}$ ) and segmented model ( $h_{\text{CF,mod}} = 352 \text{ W m}^{-2} \text{K}^{-1}$ ) results. As a result of the increased CF-to-working fluid heat transfer rates, average vapor outlet flow rates are slightly higher in the simulation (+4.1%,  $661.2 \text{ ml min}^{-1}$ ,  $4.61 \text{ kg m}^{-2} \text{s}^{-1}$ ) than predicted with the segmented model ( $635.1 \text{ ml min}^{-1}$ ,  $4.43 \text{ kg m}^{-2} \text{s}^{-1}$ ) (Fig. 10). If the average evaporative heat transfer coefficient from the simulation is specified as an input to the segmented model, overall heat transfer rates agree to within 4% ( $Q_{\text{BPG,sim}} = 18.26 \text{ W}$ ,  $Q_{\text{BPG,mod}} = 18.97 \text{ W}$ ). Outlet flow rate agreement also improves slightly for this case ( $V_{\text{L,out,sim}} = 99.8 \text{ ml min}^{-1}$  and  $V_{\text{V,out,sim}} = 661.2 \text{ ml min}^{-1}$ ;  $V_{\text{L,out,mod}} = 94.3 \text{ ml min}^{-1}$  and  $V_{\text{V,out,mod}} = 684.6 \text{ ml min}^{-1}$ ).

Results from this simulation indicate significantly higher convective flow evaporation heat transfer coefficients ( $h_{\text{evap,sim,avg}} = 1390 \text{ W m}^{-2} \text{K}^{-1}$ ) than predicted with the model of [47] ( $h_{\text{evap,mod,avg}} = 650 \text{ W m}^{-2} \text{K}^{-1}$ ):

$$h_{\text{evap,LW}} = \left[ 1 + x \text{Pr}_L \left( \frac{\rho_L}{\rho_V} - 1 \right) \right]^{0.35} \left( 0.023 \frac{k_L}{D} \text{Re}_{\text{Lo}}^{0.8} \text{Pr}_L^{0.4} \right) \quad (17)$$

Here, the quality ( $x$ ) predicted by the segmented model ranges from 0.074 to 0.118, the liquid Prandtl number is  $\text{Pr}_L = 12$ , the liquid-to-vapor density ratio is 50, and the liquid-only Reynolds number is  $\text{Re}_{\text{Lo}} = GD/\mu_L = 99$ . The resulting predicted evaporative heat transfer coefficient increases with quality from 600 to  $700 \text{ W m}^{-2} \text{K}^{-1}$  along the domain. This correlation was formulated semi-empirically using experimental flow boiling data to modify turbulent single-phase channel flow results. It is therefore possible that this formulation is not valid for the low (laminar) Reynolds number and mass flux ( $G = 38 \text{ kg m}^{-2} \text{s}^{-1}$ ) conditions considered in this study.

An alternate, flow-regime-specific, mechanistic evaporative heat transfer modeling approach was proposed in [48] for large channel diameter turbulent flows. The model of [48] applies fully developed heat transfer results for annular liquid film flow in

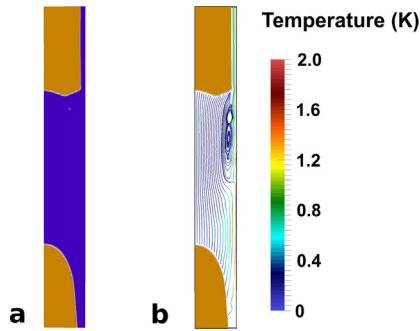


**Fig. 11.** (a) Representative liquid-slug region from evaporating flow simulation, (b) Streamlines in bubble-wake region (colored by  $T - T_{\text{sat}}$ ).

bubble regions and for channel flow in slug regions. For the laminar conditions considered in the present investigation, radial conduction heat transfer would be dominant in liquid films, and the slug region channel flow Nusselt number would be  $Nu \sim 3.7$ . The overall predicted heat transfer coefficient is:

$$h_{\text{evap,WK}} = \frac{2\beta k_L}{D \ln[D/(D - 2\delta_f)]} + \frac{3.7(1 - \beta)k_L}{D} \quad (18)$$

Here,  $\beta$  is the relative Taylor bubble length ( $\beta = L_b/(L_b + L_s)$ ) predicted using the model of [49] ( $\beta = 0.61 - 0.71$  here).  $\delta_f$  is the predicted liquid film thickness (0.52 mm). The resulting heat transfer coefficient increases from 640 to 700  $\text{W m}^{-2} \text{K}^{-1}$  along the length of the domain (Fig. 9b).

These results indicate that the mechanisms of evaporative heat transfer at these distributed-heated BPG laminar flow conditions ( $Re_j = 460 - 660$ ) may be significantly different than assumed in these two models. In particular, intense circulation in the wake regions trailing Taylor bubbles may transport more heat from the wall than would be predicted for fully developed channel flow (Fig. 11). Recently, this Taylor flow wake heat transfer enhancement effect was identified experimentally in [50].

BPGs generally operate in the intermediate Bond number regime:  $5 \lesssim Bo \lesssim 40$ , corresponding to channel diameters of

$6 \lesssim D \lesssim 17$  mm for ambient air–water flows. Liquid slugs are significantly shorter in the intermediate Bond number regime ( $L_s/D \sim 1 - 6$  [49]) than for high Bond number Taylor flows ( $L_s/D \gtrsim 16$  [51]), as considered in the flow boiling analysis of [48]. Therefore, the relative importance of bubble-wake heat transfer enhancement may be more significant for intermediate Bo. Additionally, expected thermal developing flow lengths ( $\sim 0.06 Re_j Pr_L D$ ) vary from 2.5 – 3.7 m along the length of the channel, about 200 – 400 times the predicted slug lengths. Similarly, the falling liquid film flows may not reach thermally fully developed states for the relatively short average bubble lengths found in these studies ( $L_{b,\text{avg}}/D = 3.3$ ,  $L_{b,\text{avg}}/\delta_{f,\text{avg}} = 41.7$ ). In comparison, for these conditions, the models of [52] and [53] predict falling-film thermal development lengths of  $47\delta_f$  and  $35\delta_f$ , respectively.

A representative simulation snapshot is presented in Fig. 12 to assist in the evaluation of these potential heat transfer enhancement mechanisms. As can be observed in the detail view of the liquid slug region (Fig. 12d), the bubble wake causes the wall thermal boundary layer to thin in the near-tail region before it gradually thickens in the thermally developing liquid slug bulk. Therefore, the heat transfer effect of the wake can be conceptualized and modeled as a reset of the thermal boundary layer (initiating a new developing channel flow region in each liquid slug). In contrast, the near-wall thermal boundary layer appears to continue unperturbed from the liquid slug bulk to the bubble-film region (Fig. 12c). This may occur because the rounded bubble nose permits a gradual transition between the two regions without wake effects. Therefore, developing film-flow effects are not significant. Based on these results, a modification to the mechanistic flow evaporation heat transfer coefficient model (Eq. (18)) is proposed, which accounts for each slug as a new developing channel flow region (using the results of [54] correlated by [55]).

$$Nu_{\text{DevSlug}} = 3.66 + \frac{(0.049 + 0.020/Pr_L)Gz_s^{1.12}}{1 + 0.065Gz_s^{0.7}} \quad (19)$$

$$Gz_s = \frac{D Re_j Pr_L}{L_s} \quad (20)$$

$$h_{\text{evap,DevSlug}} = \frac{2\beta k_L}{D \ln[D/(D - 2\delta_f)]} + \frac{(1 - \beta)k_L}{D} Nu_{\text{DevSlug}} \quad (21)$$

Here,  $Gz_s$  is the slug Graetz number, and increases along the length of the channel in the segmented model case from 3740 to 6670, corresponding to increasing  $Re_j$  (460–660) and decreasing liquid slug length ( $L_s = 11.4 - 9.2$  mm). The resulting average slug-region heat transfer coefficient increases from 1750 to 2200  $\text{W m}^{-2} \text{K}^{-1}$  along the channel length, and is greater than  $2\times$  times that of the fully developed liquid film ( $\sim 900 \text{ W m}^{-2} \text{K}^{-1}$ ). The overall flow-evaporation coefficient (Eq. (21)) increases from 1240 to 1270  $\text{W m}^{-2} \text{K}^{-1}$  along the length of the channel, and agrees with the linear fit to the simulation heat transfer coefficient to within 15% (AAD = 11%, Fig. 9b). The linear fit to the simulation heat transfer coefficient is skewed slightly high due to entrance and exit effects in the domain. The proposed developing slug flow model matches more closely with the linear fit to simulation data between  $z = 0.05$  and  $0.25$  m (3.5% average absolute deviation). If this proposed flow evaporation heat transfer coefficient model is used, rather than [47,48], the segmented model overall heat transfer rate increases from 15.7 W to 18.6 W, matching the simulation value (18.3 W) within 2%.

While good agreement with simulation results was obtained using the developing slug flow convective coefficient model (Eqs. (19)–(21)) in this case, further investigation into intermediate Bond number Taylor flow evaporation is needed. The proposed

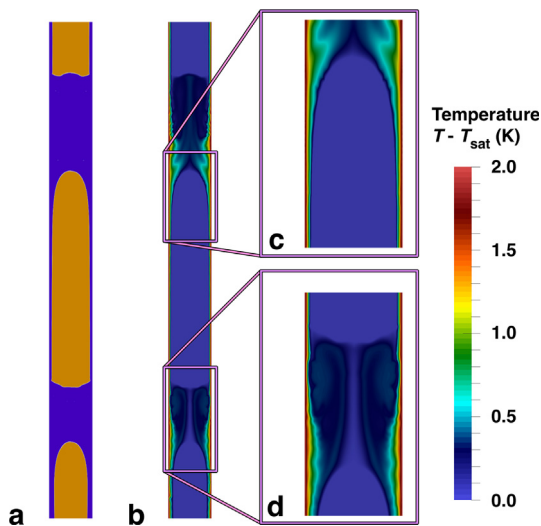


**Fig. 12.** (a) Representative phase distribution from simulation results, (b) Temperature field in region, (c) Detail view of temperature field near the bubble nose (note that the near-wall temperature profile is relatively unchanged over the slug-to-film transition), (d) Detail view of temperature field near the bubble tail (note that the thermal boundary layer thins in the wake region before it starts to thicken further into the slug).

model is specific to laminar flow, and other formulations may be needed to describe turbulent conditions. Additionally, this simulation study does not account for nucleate boiling effects, which could also modify liquid slug and film flow patterns and convection characteristics at higher wall superheats.

Even with potentially large discrepancies in  $h_{\text{evap}}$ , overall heat transfer predictions using the 1-D segmented model agreed closely with experimental results in [1] (averaged absolute deviation for  $Q = 3.7\%$ ). This occurred because BPG heat transfer was almost always limited by the CF thermal capacity rather than CF-to-working fluid thermal resistance (i.e.,  $T_{\text{CF,out}} \sim T_{\text{sat}}$ ). Additionally, single-phase CF-to-tube thermal resistance was generally predicted to be dominant due to the low thermal conductivity of the CF ( $\sim 0.1 \text{ W m}^{-1} \text{ K}^{-1}$ ) and laminar CF flow conditions. As such, large variations in working-fluid side convection resistance did not significantly affect predicted BPG behavior in that study. However, under different operating conditions, accurate prediction of flow boiling heat transfer coefficients may be critical.

The present simulation predicts slight bulk liquid superheating ( $\sim 2.4\%$  of input heat for the domain,  $T_{\text{L,out}} - T_{\text{sat}} = 0.13 \text{ K}$ ). This fraction of sensible heating would be much smaller when averaged over a full heated BPG length, and may be further decreased for the turbulent flow conditions expected in some BPGs. Thus, the slight improvement in segmented model fidelity obtained by accounting for this factor may not outweigh the cost of increased complexity.

#### 3.4. Taylor flow kinematics and hydrodynamics

Gas-phase (Taylor bubble) velocity profiles are presented in Fig. 13a from the segmented model and time-averaged simulation data. A best-fit linear trend line is also presented for the simulation data because results are not fully converged to a smooth curve after 4 ss. The segmented model velocities generally match simulation results, locally deviating from the simulation trend line by 5–7%. Axial void fraction profiles are presented in Fig. 13b for the segmented model and time-averaged simulation cases. The average absolute deviation is 2.9% indicating close agreement.

Other Taylor flow kinematic quantities (film thickness –  $\delta_f$ , Taylor bubble length –  $L_b$ , liquid slug length –  $L_s$ ) cannot be assessed locally without very long simulation times. Therefore, these quantities are compared based on full simulation domain averages. The segmented model predicts that liquid film thickness varies over  $\delta_f$

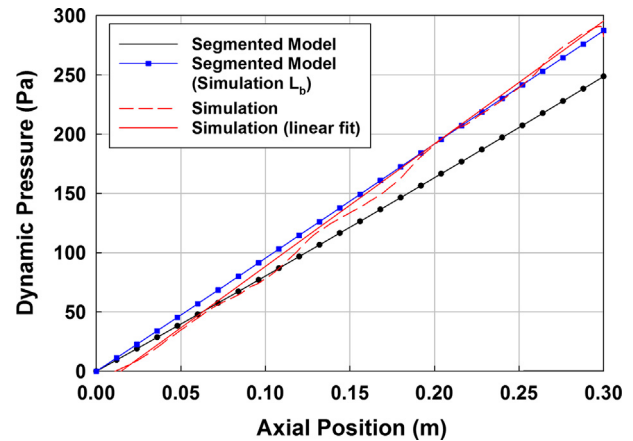


Fig. 14. Comparison of segmented model and simulation axial hydrodynamic pressure profiles.

= 0.51 – 0.53 mm along the length of the domain. This agrees relatively closely with the time- and axially averaged simulation result of  $\delta_f = 0.613 \text{ mm}$ . In the segmented model, the predicted Taylor bubble length increases from  $L_b = 17.4 - 22.3 \text{ mm}$  from the inlet to outlet. The liquid slug length decreases, correspondingly, from  $L_s = 11.4 - 9.2 \text{ mm}$ . The simulation yields average bubble and slug lengths of  $L_b = 25.5 \pm 3.8 \text{ mm}$  and  $L_s = 11.0 \pm 1.5 \text{ mm}$ . Here, uncertainties are reported as 95% confidence intervals for 141 bubble and 128 slug instances in the unsteady simulation. Thus, the simulation average slug and bubble lengths lie within the segmented model ranges. These results show reasonable agreement considering the difficulty of accurately predicting bubble and slug lengths (cf. [49]). Overall, this analysis indicates general validity of the intermediate Bond number kinematic Taylor flow sub-model employed in the segmented model (Appendix A).

Time-averaged hydrodynamic pressure gradients are presented in Fig. 14 for simulation results based on wall shear stress values ( $\nabla p_d = -4\tau_{\text{wall}}/D$ ). Somewhat paradoxically, these results predict hydrodynamic pressure recovery in the flow direction. This occurs because wall shear stress on the falling liquid films around Taylor bubbles acts in the direction of net flow (upwards). This negative dynamic pressure gradient effect has also been identified in [33,56]. For the investigated case, the Taylor bubbles are

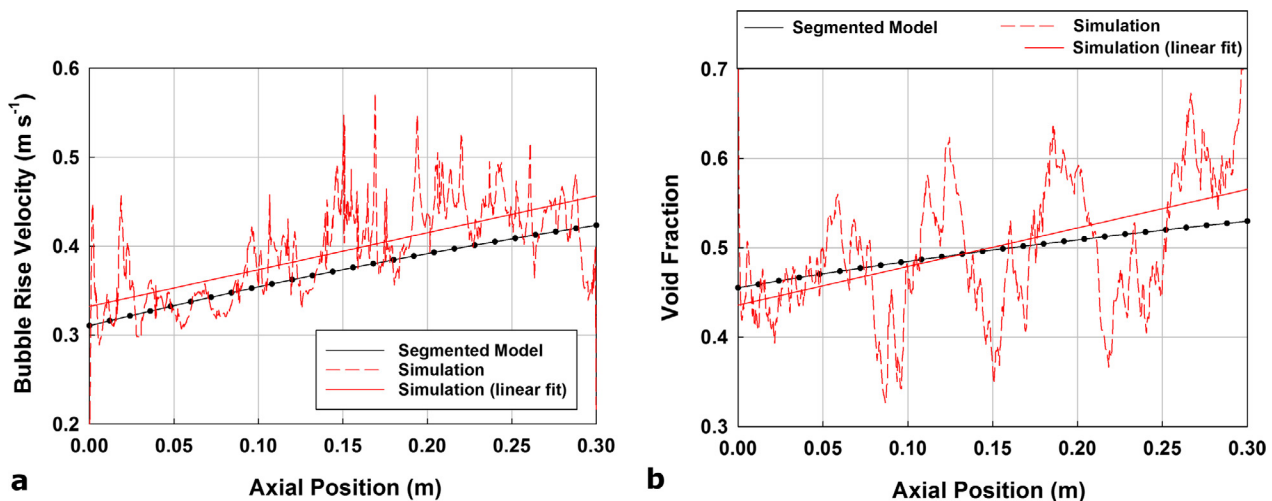


Fig. 13. Comparison of model and simulation profiles of (a) bubble rise velocity and (b) void fraction.



significantly longer than liquid slugs ( $\beta = 0.718$ ). Thus, the net hydrodynamic axial pressure gradient acts in the flow direction.

These results agree reasonably well with baseline segmented model results for dynamic pressure gradient  $\nabla p_d$  ( $\nabla p_{d,\text{sim}} = 1015 \text{ Pa m}^{-1}$ ,  $\nabla p_{d,\text{mod}} = -829 \text{ Pa m}^{-1}$ , 18% deviation). The segmented model predicts shorter Taylor bubbles ( $L_{b,\text{sim}} = 25.5 \text{ mm}$ ,  $L_{b,\text{mod}} = 17.4 - 22.2 \text{ mm}$ ), and thus, a higher frequency of bubble-to-slug flow-transition pressure losses. If the average simulation bubble length is specified as an input to the segmented model, then  $\nabla p_{d,\text{mod}} = 957 \text{ Pa m}^{-1}$  (5.7% deviation). This result provides validation for the hydrodynamic Taylor flow modeling approach employed in the segmented model. However, results are sensitive to both the unit cell length and flow transition pressure loss formulation.

#### 4. Discussion

In this investigation, direct simulations were performed for the Taylor flow evaporation process in the proposed distributed CF-heated BPG design. Results from this simulation indicate general validity of the 1-D segmented model formulated in [1] with Taylor flow closure parameters from [33]. Reasonable agreement was found between simulation and segmented model results for heat transfer and phase-change rates ( $Q_{\text{BPG}}$ , 14% deviation), bubble rise velocity ( $U_b$ , 5–7%), liquid film thickness ( $\delta_f$ , 15%), and void fraction ( $\alpha$ , 2.9%). Predictions for Taylor bubble length ( $L_b$ ) and liquid slug length ( $L_s$ ) are also relatively close between the simulation and segmented model, matching at points to within sampling uncertainty. Hydrodynamic pressure gradient predictions match within 18%. This agreement improves to 6% if the average simulation bubble lengths are specified as inputs to the segmented model instead of using the bubble length correlation of [49]. The simulation was conducted for a BPG with  $Re_f = 460$ – $660$ ,  $Pr_L = 12$ ,  $Bo = 14$ ,  $N_f = 710$ , and volumetric flow quality ( $V_v/(V_v + V_L)$ ) =  $0.8 - 0.9$ . Further simulations may be needed to confirm the segmented model applicability at significantly different BPG operating conditions.

The higher heat transfer rates found in the simulation resulted from the flow evaporation convection coefficient ( $\sim 1390 \text{ W m}^{-2} \text{ K}^{-1}$ ), which significantly exceeded values predicted with prior models ( $\sim 650 \text{ W m}^{-2} \text{ K}^{-1}$  [47],  $\sim 670 \text{ W m}^{-2} \text{ K}^{-1}$  [48]). A simple mechanistic heat transfer model that accounts for the effect of wake at the bubble-tail to slug transitions as a “reset” of the thermal boundary layer was proposed. The resulting heat transfer coefficient agrees with averaged simulation results, with an AAD of 11%. If this flow evaporation heat transfer model is employed, the overall segmented model heat transfer rate matches simulation results within 2%. However, additional research is needed to evaluate and extend this approach for other conditions, especially for turbulent flows and when nucleate boiling heat transfer is significant.

One limitation of this simulation approach is that it only resolves convective evaporation phase change, and not nucleate boiling. Nucleate boiling may be a significant mode of heat transfer for many BPG flows, particularly in the near-inlet regions where wall superheat is greatest. Therefore, future investigations of nucleate boiling effects in BPGs are recommended. Additionally, the present investigation employs 2-D axisymmetric simulations, which cannot capture potential wake effects due to asymmetry or off-axis motion of Taylor bubble tails. Future 3-D simulations could resolve such phenomena and improve understanding of wake-region heat transfer.

#### 5. Conclusions

In this investigation, a phase-change model and solver was developed for evaporating liquid–vapor flow VOF simulations.

The formulation employs a volume source splitting technique to maintain interface sharpness and ensure accurate phase-change rates. This phase-change model operates on cell values, and thus does not require geometric interface reconstruction. Validation was demonstrated for a case of horizontal film evaporation.

2-D axisymmetric simulations of distributed CF-heated BPG flow were performed. Results from this study provided confirmation of the 1-D segmented CF-heated BPG modeling approach of [1]. Close agreement was found between segmented model and simulation predictions for heat transfer rates ( $Q_{\text{BPG}}$ ), axial phase flow rate profiles ( $V_L$ ,  $V_v$ ), void fraction ( $\alpha$ ), liquid film thickness ( $\delta_f$ ), Taylor bubble and liquid slug lengths ( $L_b$ ,  $L_s$ ,  $\beta$ ), and hydrodynamic pressure gradient ( $\nabla p_d$ ). Taylor bubble wake and thermally developing flow effects were identified as causes for the high convective evaporation coefficient values found in the simulation case. A simple mechanistic model that accounted for these effects was proposed, and good agreement with simulation results was obtained.

In future studies, this approach could be applied to simulate distributed-heated BPG flows with target absorption system working fluids (e.g., ammonia–water). Such studies will necessitate greater computational resources to resolve the increased ranges of scales. Additionally, turbulence modeling for such two-phase conditions represents an open challenge. By developing a combined one-/two-fluid simulation formulation, it may be possible to simulate subcooled flow boiling phenomena. With such advances, it is expected that reconstruction-free simulations can be performed for many liquid–vapor phase-change processes of interest.

#### Acknowledgements

The authors wish to acknowledge generous financial support from the U.S. Department of Energy through the Krell Institute (Contract DE-FG02-97ER25308), and computing resources from the National Energy Research Scientific Computing Center, which is supported by the Office of Science of the U.S. Department of Energy under Contract DE-AC02-05CH11231.

#### Conflict of interest

None.

#### Appendix A. Axially segmented distributed coupling-fluid-heated bubble-pump generator model

##### A.1. Model overview

A steady-state segmented coupled fluid-flow and heat-transfer model was developed for a distributed coupling-fluid heated bubble-pump generator (BPG) in [1]. This model is adapted to analyze the saturated flow evaporation in the representative BPG and operating conditions investigated in Section 3. Refined Taylor bubble rise velocity sub-models are adopted from [33].

This co-flow tube-in-tube BPG is configured with evaporating working fluid (WF) flow in the inner tube ( $ID_i = 7.8 \text{ mm}$ ), and coupling-fluid (CF) flow in the annulus ( $OD_i = 9.5 \text{ mm}$ ,  $ID_o = 10.9 \text{ mm}$ ) (Fig. 7). The investigated BPG length is  $0.3 \text{ m}$ . In this model, the working fluid (WF) and coupling fluid (CF) channels are divided into 25 equal length axial segments. The inner-tube wall is modeled as a thermal resistance between the WF and CF channels. Mass, energy, and momentum balances are applied over each segment of the WF channel. Energy balances are applied over each segment of the uniform-flow-rate CF channel. Flow properties (e.g.,  $p$ ,  $T$ ,  $V_L$ ) are stored at nodes representing inlet and outlet

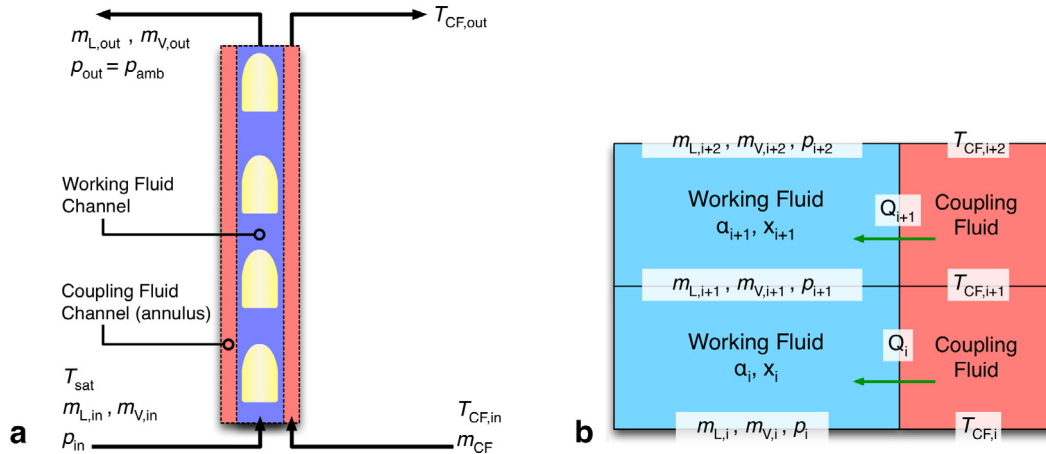


Fig. A.1. (a) Schematic and (b) discretization scheme for BPG model.

conditions for each segment. The model is implemented and solved using the Engineering Equation Solver (EES) software [57]. A schematic of the model problem and discretization scheme is presented in Fig. A.1. The model is summarized in the following sections, with representative values reported for a case with saturated ( $T = T_{\text{sat}}$ ) WF inlet liquid and vapor flow rates of  $V_L = 100 \text{ ml min}^{-1}$  and  $V_V = 400 \text{ ml min}^{-1}$ , WF outlet gage pressure of 0 Pa, coupling fluid inlet temperature of  $T_{\text{CF,in}} - T_{\text{sat}} = 10 \text{ K}$ , and CF flow rate of  $V_{\text{CF}} = 200 \text{ ml min}^{-1}$ .

#### A.2. Working-fluid mass, energy, and momentum balances

A mass balance is performed over each segment of the WF channel (i):

$$\dot{m}_{L,i} + \dot{m}_{V,i} = \dot{m}_{L,i+1} + \dot{m}_{V,i+1} \quad (\text{A.1})$$

For the representative model case, the liquid flow rate decreases from 100.0 to 95.3  $\text{ml min}^{-1}$  along the model domain. The vapor flow rate increase from 400.0  $\text{ml min}^{-1}$  at the inlet to 635.1  $\text{ml min}^{-1}$  at the outlet (outlet quality of 0.12).

Energy balances are applied over each segment of the WF channel.

$$(\dot{m}_{V,i+1} - \dot{m}_{V,i})h_{LV} = h_{\text{evap},i}A_i(T_{\text{wall}} - T_{\text{sat}}) \quad (\text{A.2})$$

Here,  $A_i$  is the WF channel segment inner area ( $2.92 \times 10^{-4} \text{ m}^2$ ) and  $h_i$  is the convective flow evaporation heat transfer coefficient of [47]. The nucleate boiling contribution to heat transfer is assumed to be small at the predicted wall superheat ( $T_{\text{wall}} - T_{\text{sat}} = 4.1$  to  $2.7 \text{ K}$ ) and is therefore neglected.

$$h_{\text{evap}} = \left[1 + xPr_L \left(\frac{\rho_L}{\rho_V} - 1\right)\right]^{0.35} \left(0.023 \frac{k_L}{D} Re_{L0}^{0.8} Pr_L^{0.4}\right) \quad (\text{A.3})$$

The predicted evaporative heat transfer coefficient increases from 600 to 700  $\text{W m}^{-2} \text{ K}^{-1}$  along the flow length. The corresponding inner channel heat flux decreases in the flow direction (2440–1860  $\text{W m}^{-2}$ ) as the heating coupling fluid temperature approaches  $T_{\text{sat}}$ .

A momentum balance is applied to each segment of the WF, accounting for pressure drop due to hydrostatic forces (fluid weight) and hydrodynamic effects (frictional flow resistance and flow-transition losses). Fluid acceleration contributions are assumed negligible.

$$p_i - p_{i+1} = \Delta p_{\text{hs},i} + \Delta p_{\text{d},i} \quad (\text{A.4})$$

The hydrostatic pressure drop in a segment of height  $H_{\text{seg},i}$  is:

$$\Delta p_{\text{hs},i} = [(1 - \alpha_i)\rho_L + \alpha\rho_V]gH_{\text{seg},i} \quad (\text{A.5})$$

Here,  $\alpha_i$  is the local void fraction (vapor phase volume fraction). The hydrostatic pressure drop is the dominant component, accounting for 1520 Pa. This is slightly more than the total pressure drop (1260 Pa), because frictional flow resistance in the draining liquid films around Taylor bubbles ( $-440 \text{ Pa}$ ) exceeds other hydrodynamic pressure drop contributions (200 Pa). Accurate prediction of the void fraction ( $\alpha$ ) and hydrodynamic pressure drop gradient ( $\nabla p_{\text{d},i} = \Delta p_{\text{d},i}/H_{\text{seg},i}$ ) requires flow-regime specific modeling, and is described in the next section.

#### A.3. Two-phase Taylor flow model

The two-phase flow sub-model takes, as inputs, the channel geometry ( $D$ ), liquid and vapor axial flow rates (volumetric flow rates  $V_L$  and  $V_V$ , or equivalently, superficial velocities  $j_L$  and  $j_V$ ), and thermophysical fluid properties. It returns the local void fraction ( $\alpha$ ) and hydrodynamic pressure gradient ( $\nabla p_d$ ), yielding closure of the segmented momentum equation (Eq. (A.4)). The modeling approach employed here is specific to the two-phase flow characteristics expected in distributed heated BPGs in which the flow pattern is primarily intermediate Bond number Taylor flow ( $5 \leq Bo \leq 40$ ). The model idealizes Taylor flow assuming repeating identical *unit cells*, each comprised of a liquid slug and cylindrical Taylor bubble. Continuity in each unit cell requires equal volumetric fluxes through cross-sections of the bubble and liquid slug portions. Assuming uniform velocity profiles in the liquid slug ( $U_s$ ), Taylor bubble ( $U_b$ ), and liquid film ( $U_f$ ):

$$U_s = j = \alpha_b U_b + (1 - \alpha_b)U_f \quad (\text{A.6})$$

Here  $\alpha_b$  is the void fraction in the portion of the unit cell from the tail to nose of the Taylor bubble. At the inner-tube outlet in the representative case,  $\alpha_b = 0.748$ , and the bubble diameter is 6.70 mm ( $ID_i = 7.75 \text{ mm}$ ). At this same point, the model predicts:  $U_s = 0.258 \text{ m s}^{-1}$ ,  $U_b = 0.424 \text{ m s}^{-1}$ , and  $U_f = -0.232 \text{ m s}^{-1}$  (i.e., downward flow).

Additionally, continuity requires that the upward vapor flow rate in the portion of the unit cell containing the Taylor bubble ( $\beta = L_b/(L_s + L_b)$ ) equals the total vapor flow rate.

$$j_V = \beta\alpha_b U_b \quad (\text{A.7})$$

The total unit-cell void fraction is thus:

$$\alpha = \beta\alpha_b \quad (\text{A.8})$$

In the representative model case,  $\alpha$  and  $\beta$  increase along the WF channel and reach outlet values of 0.530 and 0.709, respectively.

The Taylor bubble rise velocity model of [33] is adopted here. This model incorporates capillary-scale [58] and large-channel-scale results [59,60], and was validated for intermediate Bond number flows.

$$U_b = C_0 j + \Gamma \sqrt{gD} \quad (\text{A.9})$$

$$C_0 = f_{LS} C_{0,LS} + (1 - f_{LS}) C_{0,Ca} \quad (\text{A.10})$$

$$f_{LS} = \left( \frac{1}{1 + (Bo/12.3)^{-0.88}} \right)^{[(Re_j/5900)^{-0.27}]} \quad (\text{A.11})$$

$$C_{0,LS} = 1.20 + \frac{1.09}{1 + (Re_j/805)^4} \quad (\text{A.12})$$

$$C_{0,Ca} = \frac{1}{1 - 0.61 Ca^{0.33}} \quad (\text{A.13})$$

$$\Gamma = \begin{cases} 0.344 \left[ 1 - \exp\left(\frac{-0.01 N_f}{0.345}\right) \right] \\ \sqrt{1 + \frac{20}{Bo} - \frac{93.7}{Bo^2} - \frac{676.5}{Bo^3} + \frac{2706}{Bo^4} \frac{1 - 0.96 \exp(-0.0165 Bo)}{1 - 0.52 \exp(-0.0165 Bo)}} & Bo > 4.55 \\ 0 & Bo \leq 4.55 \end{cases} \quad (\text{A.14})$$

$$Re_j = \frac{\rho_L j D}{\mu_L} \quad Bo = \frac{(\rho_L - \rho_G) g D^2}{\sigma} \quad (\text{A.15})$$

$$Ca = \frac{\mu_L j}{\sigma} \quad N_f = \sqrt{\frac{\rho_L (\rho_L - \rho_G) g D^3}{\mu_L^2}} \quad (\text{A.15})$$

Here  $Re_j$  is the liquid slug Reynolds number (670 at the outlet),  $Bo$  is the Bond number (14.4),  $Ca$  is the capillary number (0.0194 at the outlet), and  $N_f$  is a measure of relative gravitational-to-viscous forces (712). For the representative case, the predicted bubble rise velocity increases from 0.310 to 0.424 m s<sup>-1</sup> along the channel length.

Laminar liquid flow is assumed in the falling film, and interfacial shear is accounted for.

$$U_f = \frac{4}{\pi [D^2 - (D - 2\delta_f)^2]} \int_{D/2 - \delta_f}^{D/2} (2\pi r) \left\{ \frac{g(\rho_L - \rho_G)}{4\mu_L} \left[ \left( \frac{D}{2} \right)^2 - r^2 + 2 \left( \frac{D}{2} - \delta_f \right)^2 \ln \left( \frac{2r}{D} \right) \right] + \frac{\tau_{int}(D/2 - \delta_f)}{\mu_L} \ln \left( \frac{2r}{D} \right) \right\} dr \quad (\text{A.16})$$

$$f_b = \frac{4}{Re_b} \left\{ \frac{3.44}{\sqrt{L_b^*}} + \left[ \frac{1.25}{4L_b^*} + 16 - \frac{3.44}{\sqrt{L_b^*}} \right] / [1 + 0.00021 (L_b^*)^{-2}] \right\} \quad (\text{A.17})$$

$$Re_b = \frac{\rho_G (U_b - U_f) D_b}{\mu_G} \quad L_b^* = \frac{L_b}{Re_b D_b} \quad (\text{A.18})$$

$$\tau_{int} = \frac{f_b}{8} \rho_G (U_b - U_f)^2 \quad (\text{A.19})$$

A developing laminar flow model is employed to determine the bubble friction factor (Eqs. (A.17)–(A.19) [55]). The laminar flow assumption is applied because  $240 < Re_b < 290$  for this case. The film thickness ( $\delta_f$ ) and bubble region void fraction ( $\alpha_b = (D - 2\delta_f)^2/D^2$ ) are determined by substitution of the film mean velocity (Eq. (A.16)) into the continuity constraint (Eq. (A.6)). For the representative case, liquid-film thickness varies over 0.515 – 0.525. The frictional pressure gradient due to film-to-wall shear around the Taylor bubbles is:

$$\tau_{int}(\pi D_b) - \tau_w(\pi D) = \frac{\pi}{4} (D^2 - D_b^2) (\rho_L - \rho_G) g \quad (\text{A.20})$$

$$\nabla p_{f,b} = \frac{4\tau_{wall}}{D} \quad (\text{A.21})$$

This pressure gradient is negative because it acts in the bulk flow direction (upward), opposing the downward flowing film, and approaches  $-870 \text{ Pa m}^{-1}$  at the BPG outlet.

Average Taylor bubble lengths in each segment are estimated using the correlation proposed in [49] for intermediate Bond number flow.

$$\frac{L_b}{D} = 1.813 \left\{ \exp \left[ 1.815 - 0.866 \left( \frac{U_b}{j} \right)^{2.176} \right] \left( \frac{\alpha}{1 - \alpha} \right)^{1.637} + 1 \right\} \quad (\text{A.22})$$

For the representative case, this yields  $L_b = 22.3 \text{ mm}$  ( $2.1 \times D$ ) at the BPG outlet. At that point,  $\beta = L_b/(L_b + L_s) = 0.709$ ; therefore, liquid slugs are predicted to only be  $L_s = 9.2 \text{ mm}$  ( $1.2 \times D$ ).

Frictional resistance in the liquid slug is evaluated using the universal (laminar-to-turbulent) channel flow correlation of [61]. In this case, the slug Reynolds number ( $Re_j$ ) increases from 460 to 660.

$$f_s = 8 \left\{ \left( \frac{8}{Re_j} \right)^{12} + \left[ 2.457 \ln \left( \frac{1}{(7/Re_j)^{0.9}} \right) + \left( \frac{3750}{Re_j} \right)^{16} \right]^{-1.5} \right\}^{1/12} \quad (\text{A.23})$$

$$\nabla p_{f,s} = f_s \frac{\rho_L j^2}{2D} \quad (\text{A.24})$$

The predicted liquid-slug frictional pressure gradient approaches  $410 \text{ Pa m}^{-1}$  at the WF outlet.

Bubble-to-slug flow transition pressure drops are estimated using the model proposed by [1], which extends the capillary scale model of [62] to higher Reynolds number conditions.

$$\Delta p_{trans} = \frac{1}{2} \frac{\rho_L j^2}{Re_j^{2/3} Ca^{1/3}} \left( 10.88 + \frac{60}{1 + (Re_{j,L}/800)^{-2}} \right) \quad (\text{A.25})$$

$$Re_{j,L} = \frac{\rho_L j L}{\mu_L} \quad (\text{A.26})$$

In the representative case, the predicted flow transition pressure drop per unit cell increases from 13 Pa to 19 Pa along the channel.

The liquid film, liquid slug, and transition pressure drops are combined to yield the hydrodynamic pressure drop in each segment:

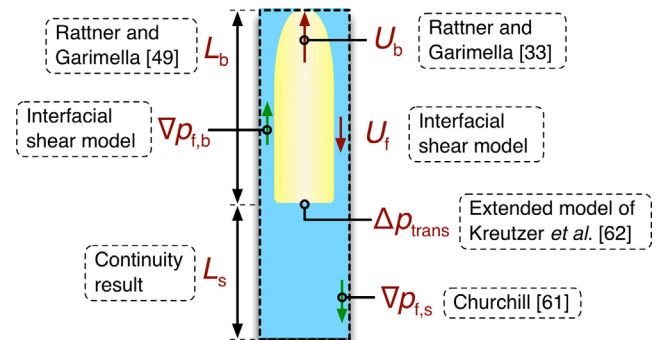


Fig. A.2. Schematic summary of mechanistic Taylor-flow model.

$$\frac{\Delta p_{d,i}}{H_{seg,i}} = \beta \nabla p_{f,b,i} + (1 - \beta) \nabla p_{f,s,i} + \frac{\beta}{L_b} \Delta p_{trans} \quad (A.27)$$

The net hydrodynamic pressure drop gradient ( $\nabla p_d$ ) varies from  $-790$  to  $-870$  Pa along the channel length (i.e., acting in the bulk flow direction). A schematic summary of the developed Taylor flow model is presented in Fig. A.2.

#### A.4. Coupling-fluid channel model

The CF flow is modeled as single-phase fluid flow with constant thermophysical properties (Table 2). The annular-flow fully developed laminar ( $Re_{CF} = 33$ ) heat-transfer coefficient ( $h_{CF} = 350 \text{ W m}^{-2} \text{ K}^{-1}$ ) was evaluated using a built-in Engineering Equation Solver function [57]. The heat transfer rate and inside tube-wall temperature ( $T_{wall,i}$ ) in each segment are evaluated using a thermal resistance-network model:

$$q_i(\pi D) = \frac{T_{CF,i+1} - T_{wall,i}}{\frac{1}{h_{CF}(\pi D_{a,i})} + \frac{\ln(D_{a,o}/D_{a,i})}{2\pi k_t}} = \frac{T_{CF,i+1} - T_{wall,i}}{R'_{CF} + R'_t} \quad (A.28)$$

Here the CF convection resistance ( $R'_{CF} = 0.095 \text{ m K W}^{-1}$ ) dominates the conduction resistance through the stainless-steel tube wall ( $k_{wall} = 14 \text{ W m}^{-1} \text{ K}^{-1}$ ,  $R'_t = 0.002 \text{ m K W}^{-1}$ ). A down-winding scheme ( $T_{CF,i+1} - T_{wall,i}$ ) is employed to avoid oscillations in the CF temperature distribution.

The energy balance for each segment of the coupling fluid channel is:

$$(T_{CF,i} - T_{CF,i+1})(\dot{m}_{CF} c_{p,CF}) = L_{seg,i} \frac{T_{CF,i+1} - T_{wall,i}}{R'_{CF} + R'_t} \quad (A.29)$$

In the representative case, the CF temperature decreases from  $T_{CF} = 10 \text{ K}$  at the BPG inlet, to  $7.1 \text{ K}$  at the outlet.

## References

- [1] A.S. Rattner, S. Garimella, Coupling-fluid heated bubble pump generators: experiments and model development, *UHVC Sci. Technol. Built Environ.* 21 (2015) 332–347.
- [2] J.M. Belman-Flores, J.L. Rodriguez-Munoz, C. Rubio-Maya, J.J. Ramirez-Minguela, V. Perez-Garcia, Energetic analysis of a diffusion-absorption system: a bubble pump under geometrical and operational conditions effects, *Appl. Therm. Eng.* 71 (2014) 1–10.
- [3] M. Pfaff, R. Saravanan, M.P. Maiya, S.S. Murthy, Studies on bubble pump for a water-lithium bromide vapour absorption refrigerator, *Int. J. Refrig.* 21 (1998) 452–462.
- [4] U. Jakob, U. Eicker, D. Schneider, A.H. Taki, M.J. Cook, Simulation and experimental investigation into diffusion absorption cooling machines for air-conditioning applications, *Appl. Therm. Eng.* 28 (2008) 1138–1150.
- [5] P. Srihirin, S. Aphornratana, S. Chungpaibulpatana, A review of absorption refrigeration technologies, *Renew. Sustain. Energy Rev.* 5 (2001) 343–372.
- [6] N. Dammak, B. Chaouachi, S. Gabsi, M. Bourouis, Optimization of the geometrical parameters of a solar bubble pump for absorption-diffusion cooling systems, *Am. J. Eng. Appl. Sci.* 3 (2010) 693–698.
- [7] C.W. Hirt, B.D. Nichols, Volume of Fluid (VOF) method for the dynamics of free boundaries, *J. Comput. Phys.* 39 (1981) 201–225.
- [8] M. Sussman, P. Smereka, S. Osher, A level set approach for computing solutions to incompressible two-phase flow, *J. Comput. Phys.* 114 (1994) 146–159.
- [9] S.O. Unverdi, G. Tryggvason, A front-tracking method for viscous, incompressible, multi-fluid flows, *J. Comput. Phys.* 100 (1992) 25–37.
- [10] A.S. Rattner, S. Garimella, Simple mechanistically consistent formulation for volume-of-fluid based computations of condensing flows, *J. Heat Transfer.* 136 (2014).
- [11] M. Nabil, A.S. Rattner, InterThermalPhaseChangeFoam-A framework for two-phase flow simulations with thermally driven phase change, *SoftwareX.* 5 (2016) 216–226.
- [12] A.D. Delano, Design and analysis of the Einstein refrigeration cycle Ph.D. Thesis, Georgia Institute of Technology, Atlanta, GA, 1998.
- [13] S. van der Walt, The Design and Optimization of a Bubble Pump for an Aqua-Ammonia Diffusion Absorption Heat Pump Ph.D. Thesis, North-West University, Potchefstroom, South Africa, 2012.
- [14] A. Koyfman, M. Jelinek, A. Levy, I. Borde, An experimental investigation of bubble pump performance for diffusion absorpti on refrigeration system with organic working fluids, *Appl. Therm. Eng.* 23 (2003) 1881–1894.
- [15] S.J. White, Bubble pump design and performance M.S. Thesis, Georgia Institute of Technology, Atlanta, GA, 2001.
- [16] A. Benhimidene, B. Chaouachi, S. Gabsi, M. Bourouis, Modelling of heat flux received by a bubble pump of absorption-diffusion refrigeration cycles, *Heat Mass Transf.* 47 (2011) 1341–1347.
- [17] A. Benhimidene, B. Chaouachi, S. Gabsi, A review of bubble pump technologies, *J. Appl. Sci.* 10 (2010) 1806–1813.
- [18] B. Končar, E. Krepper, Y. Egorov, CFD modeling of subcooled flow boiling for nuclear engineering applications, in: *Nucl. Energy New Eur.*, Bled, Slovenia, 2005.
- [19] E. Krepper, B. Koncar, Y. Egorov, CFD modelling of subcooled boiling - concept, validation and application to fuel assembly design, *Nucl. Eng. Des.* 237 (2007) 716–731.
- [20] R. Garma, Y. Stiriba, M. Bourouis, A. Bellagi, Numerical investigations of the heating distribution effect on the boiling flow in bubble pumps, *Int. J. Hydrogen Energy.* 39 (2014) 15256–15260.
- [21] S.W. Jo, S.A. Sherif, W.E. Lear, Numerical simulation of saturated flow boiling heat transfer of ammonia/water mixture in bubble pumps for absorption-diffusion refrigerators, *J. Therm. Sci. Eng. Appl.* 6 (2014).
- [22] C. Kunkelmann, P. Stephan, CFD simulation of boiling flows using the volume-of-fluid method within OpenFOAM, *Numer. Heat Transf.* 56 (2009) 631–646.
- [23] G. Son, V.K. Dhir, Numerical simulation of nucleate boiling on a horizontal surface at high heat fluxes, *Int. J. Heat Mass Transf.* 51 (2008) 2566–2582.
- [24] A. Esmaeili, G. Tryggvason, Computations of film boiling. Part I: numerical method, *Int. J. Heat Mass Transf.* 47 (2004) 5451–5461.
- [25] S.P. Zhang, M.J. Ni, H.Y. Ma, VOF Method for Simulation of Multiphase Incompressible Flows With Phase Change, in: *Int. Conf. Fluid Mech.*, American Institute of Physics, Guangzhou, China, 2011, pp. 579–581.
- [26] D. Bothe, H.J. Warnecke, VOF-simulation of rising air bubbles with mass transfer to the ambient liquid, in: *10th Work. Transp. Phenom. Two-Phase Flow*, 2005: pp. 61–72.
- [27] S.S. Jeon, S.J. Kim, G.C. Park, CFD simulation of condensing vapor bubble using VOF model, *World Acad. Sci. Eng. Technol.* 60 (2009) 209–215.
- [28] H. Marschall, K. Hinterberger, C. Schuler, F. Habla, O. Hinrichsen, C. Schüller, F. Habla, O. Hinrichsen, C. Schuler, F. Habla, O. Hinrichsen, Numerical simulation of species transfer across fluid interfaces in free-surface flows using OpenFOAM, *Chem. Eng. Sci.* 78 (2012) 111–127.
- [29] A. Mukherjee, S.G. Kandlikar, Numerical simulation of growth of a vapor bubble during flow boiling of water in a microchannel, *Microfluid. Nanofluid.* 1 (2005) 137–145.
- [30] Z. Yang, X.F. Peng, P. Ye, Numerical and experimental investigation of two phase flow during boiling in a coiled tube, *Int. J. Heat Mass Transf.* 51 (2008) 1003–1016.
- [31] C. Fang, M. David, A. Rogacs, K. Goodson, Volume of fluid simulation of boiling two-phase flow in a vapor-venting microchannel, *Front. Heat Mass Transf.* 1 (2010).
- [32] The OpenFOAM Foundation, OpenFOAM 2.4.0, 2015.
- [33] A.S. Rattner, S. Garimella, Taylor flow in intermediate diameter channels: simulation and hydrodynamic models, *Int. J. Heat Mass Transf.* 103 (2016) 1108–1124.
- [34] H.G. Weller, Derivation, modelling, and solution of the conditionally averaged two-phase flow equations, Nabla Ltd. Technical Report TR/HGW/02., United Kingdom, 2002.
- [35] K. Kissling, J. Springer, H. Jasak, S. Schutz, K. Urban, M. Piesche, S. Schütz, K. Urban, M. Piesche, A coupled pressure based solution algorithm based on the volume-of-fluid approach for two or more immiscible fluids, in: *V Eur. Conf. Comput. Fluid Dyn.*, Lisbon, Portugal, 2010.
- [36] H.G. Weller, G. Tabor, H. Jasak, C. Fureby, A tensorial approach to computational continuum mechanics using object-oriented techniques, *Comput. Phys.* 12 (1998) 620–631.
- [37] R.I. Issa, Solution of the implicit discretized fluid flow equations by operator splitting, Report, Imperial College, London, UK, 1982.
- [38] S.V. Patankar, Numerical Heat Transfer and Fluid Flow, Taylor & Francis Group, New York, NY, 1980.
- [39] D. Juric, G. Tryggvason, Computations of boiling flows, *Int. J. Multiph. Flow.* 24 (1998) 387–410.
- [40] Y.J. Tao, X.L. Huai, Z.G. Li, T. Yu-Jia, H. Xiu-Lan, L. Zhi-Gang, Numerical simulation of vapor bubble growth and heat transfer in a thin liquid film, *Chinese Phys. Lett.* 26 (2009) 74701.
- [41] R. Thiele, Modeling of Direct Contact Condensation With OpenFOAM M.S. Thesis, Royal Institute of Technology, Stockholm, Sweden, 2010.
- [42] S. Hardt, F. Wondra, Evaporation model for interfacial flows based on a continuum-field representation of the source terms, *J. Comput. Phys.* 227 (2008) 5871–5895.
- [43] R. Gupta, D.F. Fletcher, B.S. Haynes, On the CFD modelling of Taylor flow in microchannels, *Chem. Eng. Sci.* 64 (2009) 2941–2950.
- [44] E.J. Davis, G.H. Anderson, The incipience of nucleate boiling in forced convection flow, *AIChE J.* 12 (1966) 774–780.
- [45] S.F. Kistler, Hydrodynamics of wetting, in: J. Berg (Ed.), *Wettability*, Marcel Dekker Inc, New York, 1993, pp. 311–420.
- [46] E. Berberovic, interFoamKistler (computer program), (2008).
- [47] Z. Liu, R.H.S. Winterton, A general correlation for saturated and subcooled flow boiling in tubes and annuli, based on a nucleate pool boiling equation, *Int. J. Heat Mass Transf.* 34 (1991) 2759–2766.
- [48] V. V. Wadekar, D.B.R. Kenning, Flow boiling heat transfer in vertical slug and churn flow region, in: *Int. Heat Transf. Conf.*, Jerusalem, Israel, 1990.
- [49] A.S. Rattner, S. Garimella, Vertical upward intermediate scale Taylor flow: experiments and kinematic closure, *Int. J. Multiph. Flow.* 75 (2015) 107–123.



- [50] A. Scammell, J. Kim, Heat transfer and flow characteristics of rising Taylor bubbles, *Int. J. Heat Mass Transf.* 89 (2015) 379–389.
- [51] Y. Taitel, D. Barnea, A.E. Dukler, Modelling flow pattern transitions for steady upward gas-liquid flow in vertical tubes, *AIChE J.* 26 (1980) 345–354.
- [52] J. Mitrović, Der Wärmeaustausch am Berieselungskühler, *Brennstoff-Wärme-Kraft*. 40 (1988) 243–249.
- [53] V.V. Lel, F. Al-Sibai, R. Kneer, Thermal entry length and heat transfer phenomena in laminar way falling films, *Microgravity Sci. Technol.* 21 (2009) 215–220.
- [54] R.W. Hornbeck, An all-numerical method for heat transfer in the inlet of a tube, *Am. Soc. Mech. Eng.* 88 (1965), Paper 65-WA/HT-36.
- [55] R.K. Shah, A.L. London, *Laminar Flow Forced Convection in Ducts*, Academic Press, New York, 1978.
- [56] A. Al-Sarkhi, E. Pereyra, C. Saricha, F. Alruhaimani, Positive frictional pressure gradient in vertical gas-high viscosity oil slug flow, *Int. J. Heat Fluid Flow*. 59 (2016) 50–61.
- [57] S.A. Klein, *Engineering Equation Solver*, Version 9 (2014) F-Chart Software, Madison, WI.
- [58] H. Liu, C.O. Vandu, R. Krishna, Hydrodynamics of Taylor flow in vertical capillaries: flow regims, bubble rise velocity, liquid slug length, and pressure drop, *Ind. Eng. Chem. Res.* 44 (2005) 4884–4897.
- [59] E.T. White, R.H. Beardmore, The rise velocity of single cylindrical air bubbles through liquids contained in vertical tubes, *Chem. Eng. Sci.* 17 (1962) 351–361.
- [60] K.H. Bendiksen, On the motion of long bubbles in vertical tubes, *Int. J. Multiph. Flow*. 11 (1985) 797–812.
- [61] S.W. Churchill, Friction-factor equation spans all fluid-flow regimes, *Chem. Eng.* 84 (1977) 91–92.
- [62] M.T. Kreutzer, F. Kapteijn, J.A. Moulijn, C.R. Kleijn, J.J. Heiszwolf, Inertial and interfacial effects on pressure drop of Taylor flow in Capillaries, *AIChE J.* 51 (2005) 2428–2440.